

Relativistic Hadron-Hadron Collisions in the Ultra-Relativistic Quantum Molecular Dynamics Model

M. Bleicher^{a,e*}, E. Zabrodin^{a,d}, C. Spieles^{b,f}, S.A. Bass^{c,f}, C. Ernst^a, S. Soff^{a,e},
L. Bravina^{a,d,g}, M. Belkacem^{a,g}, H. Weber^a, H. Stöcker^a, W. Greiner^a

^a *Institut für Theoretische Physik, J. W. Goethe-Universität,
60054 Frankfurt am Main, Germany*

^b *Nuclear Science Division,
Lawrence Berkeley National Laboratory,
Berkeley, CA 94720, USA*

^c *Department of Physics, Duke University,
Durham, N.C. 27708-0305, USA*

^d *Institute for Nuclear Physics,
Moscow State University,
119899 Moscow, Russia*

arXiv:hep-ph/9909407 v1 16 Sep 1999

^e Fellow of the Josef Buchmann Foundation

^f Feodor Lynen Fellow of the Alexander v. Humboldt Foundation

^g Fellow of the Alexander v. Humboldt Foundation

*E-mail: bleicher@th.physik.uni-frankfurt.de

Abstract

Hadron-hadron collisions at high energies are investigated in the Ultra-relativistic-Quantum-Molecular-Dynamics approach. This microscopic transport model describes the phenomenology of hadronic interactions at low and intermediate energies ($\sqrt{s} < 5$ GeV) in terms of interactions between known hadrons and their resonances. At higher energies, $\sqrt{s} > 5$ GeV, the excitation of color strings and their subsequent fragmentation into hadrons dominates the multiple production of particles in the UrQMD model. The model shows a fair overall agreement with a large body of experimental h-h data over a wide range of h-h center-of-mass energies. Hadronic reaction data with higher precision would be useful to support the use of the UrQMD model for relativistic heavy ion collisions. PACS: 24.10.Lx, 13.75.-n, 13.85.-t

I. MOTIVATION

Relativistic heavy ion collision experiments at the BNL-AGS (Au(10.7 AGeV)+Au) and at the CERN-SPS (Pb(160 AGeV)+Pb) have yielded a large variety of fascinating data. Various observables like the strong J/Ψ suppression, enhanced yield of intermediate mass dilepton pairs, enhanced (anti-)hyperon yields, the creation of antimatter clusters and strong transverse flow seem to indicate the formation of very dense and highly excited matter [1]. Since these observables are connected in a non-trivial way it is a tempting task for theoreticians to model high energy heavy ion collisions in a consistent way and simultaneously predict this wide range of observables from a few hundred MeV up to several thousand GeV per nucleon at LHC.

Bear in mind, however, that up to now there is no unique theoretical description of the underlying hadron–hadron interactions, with their vastly different characteristics at different incident energies and in different kinematic intervals. Perturbative quantum chromodynamics (pQCD) can be applied to describe hard processes, i.e. processes with large four-momentum, Q^2 , transfer. But pQCD is formally inappropriate for the description of the soft interactions because of the absence of the large Q^2 –scale. Therefore, low- p_T collisions are described in terms of phenomenological models.

Early on, multiple production of secondaries in relativistic hadronic collisions has been described within the hydrodynamic approach [2]. Then Regge theory [3] and multiperipheral models have been developed to understand the phenomenology of the soft interactions. They avoid the difficulties attributed to the statistical models. An inconvenient point of this approach is the large number of free parameters, which have to be fixed by comparison to experiment. Subsequently, various QCD-motivated quark–parton models have been introduced.

Consequently, a vast variety of models for hadronic- and nuclear collisions have been developed. They may be subdivided into macroscopic (statistical and hydrodynamical) models [4] and microscopic (string-, transport-, cascade-, etc.) models like, e.g. UrQMD [5], which is applied in the present paper, FRITIOF [6], VENUS [7], QGSM [8], RQMD [9] and others [10–13] including the parton cascade approach [14]. In the hydrodynamical (thermal) model one assumes local (global) equilibrium - the dynamics is characterized by the equation of state employed. The microscopic models describe subsequent individual hadron–hadron collisions.

For low and intermediate energies hadron–hadron and nucleus–nucleus collisions are described in terms of the interactions between hadrons and their excited states, resonances, i.e. on the (quasi-)particle level. At high energies the quark and gluon degrees of freedom cannot be neglected. Then the concept of color string excitations is introduced with their subsequent fragmentation into hadrons. In lead–on–lead collisions at the full SPS energy one finds in the UrQMD model that the ten most frequent hadron–hadron collision types namely, $N\pi$, $\pi\pi$, $\Delta\pi$, NN , $\pi\rho$, $N\Delta$, πK , $\pi\eta$, $\pi\omega$, $\bar{K}\pi$ (in decreasing order of frequency) describe only 50% of the total h-h collisions. The inclusion of an additional 120 h-h collision types allows modeling up to 90% of the collisions predicted in the UrQMD model, while several thousand different h-h combinations are needed to cover more than 99% of the total number of h-h collisions.

Since only a few of these cross sections are measured, one relies heavily on extrapolations

(and transformation, e.g. via the detailed balance principle) of known processes. Therefore, here we want to present and analyze the detailed elementary h-h input used in the transport model UrQMD. The h-h predictions are a necessary basis for our understanding of the dynamics of the complex heavy ion reactions.

This paper is structured as follows: a brief description of the basic principles of the UrQMD model is given in Sec. II. Section III presents UrQMD-results of the different h-h cross-sections for different reactions and a comparison with the available experimental data. The additive quark model (AQM) is used to calculate unknown cross-sections. UrQMD is the first microscopic model which attempts to include the color coherent phenomena. The implications of the effects of color opacity and color transparency in the model are discussed. The treatment of the formation and decay of resonances and strings is described in detail in Sec. IV. The importance of finite size effects in the fragmentation of strings is demonstrated. Section V discusses the generation of the transverse momentum of particles in the model. In Sec. VI several predictions of observables for elementary channels are presented, which are especially interesting for the upcoming proton-proton run of the NA49 collaboration. Finally, a summary and conclusions are given.

II. THE URQMD APPROACH

The UrQMD-model [5] is a microscopic transport theory based on the covariant propagation of all hadrons on classical trajectories in combination with stochastic binary scatterings, color string formation and resonance decay. It represents a Monte Carlo solution of a large set of coupled partial integro-differential equations for the time evolution of the various phase space densities $f_i(x, p)$ of particle species $i = N, \Delta, \Lambda$, etc., which non-relativistically assumes the Boltzmann form:

$$\frac{df_i(x, p)}{dt} \equiv \frac{\partial p}{\partial t} \frac{\partial f_i(x, p)}{\partial p} + \frac{\partial x}{\partial t} \frac{\partial f_i(x, p)}{\partial x} + \frac{\partial f_i(x, p)}{\partial t} = \text{St}f_i(x, p) \quad , \quad (1)$$

where x and p are the position and momentum of the particle, respectively, and $\text{St}f_i(x, p)$ denotes the collision (or rather source-) term of these particle species, which are connected to any other particle species f_k .

The exchange of electric and baryonic charge, strangeness and four momentum in the t -channel is considered for baryon-baryon (BB) collisions at low energies, while meson-baryon (MB) and meson-meson (MM) interactions are treated via the formation and decay of resonances, i.e. the s -channel reactions. t -channel reactions for MB and MM collisions are taken into account from $\sqrt{s} > 3$ GeV on increasing to the only MB, MM interaction type above $\sqrt{s} = 6$ GeV. For nucleus-nucleus collisions the soft binary and ternary interactions between nucleons can be described by the real part of the in-medium G-Matrix, which is approximated by a non-relativistic density-dependent Skyrme potential of the form

$$V^{Sk} = \frac{1}{2!} t_1 \sum_{i \neq j} \delta(\vec{x}_i - \vec{x}_j) + \frac{1}{3!} t_2 \sum_{i \neq j \neq k} \delta(\vec{x}_i - \vec{x}_j) \delta(\vec{x}_j - \vec{x}_k) \quad , \quad (2)$$

where \vec{x}_α denotes the coordinate variable in the quantum phase space. The first term simulates the attractive potential of the NN-interaction, and the second one yields the

saturation. In addition, Yukawa and Coulomb potentials are implemented in the model. The potentials allow to calculate the equation of state of the interacting many body system, as long as it is dominated by nucleons. Note that these potential interactions are only used in the model for baryons/nucleons with relative momenta Δp of less than $2 \text{ GeV}/c$. For the hadronic collisions discussed here, the potential interactions are omitted. Further details of the application of the UrQMD model to heavy-ion reactions may be found in [5].

This framework allows to bridge with one concise model the entire available range of energies from the SIS energy region ($\sqrt{s} \approx 2 \text{ GeV}$) to the RHIC energy ($\sqrt{s} = 200 \text{ GeV}$). At the highest energies, a huge number of different particle species can be produced. The model should allow for subsequent rescatterings. The collision term in the UrQMD model includes more than fifty baryon species and five meson nonetts (45 mesons). The baryons and baryon resonances included in the UrQMD are listed in Table I. In addition, their antiparticles have been implemented using charge-conjugation to assure full baryon-antibaryon symmetry. Figures 1 and 2 depict the implemented meson multiplets: pseudo-scalar, vector, scalar, pseudo-vector and (not shown in the Figs.) the tensor mesons as well as the heavy vector meson resonances $\rho(1450)$, $\rho(1700)$, $\omega(1420)$, and $\omega(1600)$. Extremely heavy meson resonances ($m > 2 \text{ GeV}$) are not explicitly implemented, however they may be important when investigating, e.g. the dynamics of $\Phi\Phi$ correlations in future experiments.

All particles can be produced in hadron-hadron collisions and can interact further with each other. The different decay channels all nucleon-, Δ - and hyperon-resonances up to $2.25 \text{ GeV}/c^2$ mass as well as the meson (e.g. K^*) decays etc. are implemented. At higher energies we take advantage of the hadron universality and use a string model for the decay of intermediate states. The cross-sections of various hadronic processes as well as the formation and fragmentation of the strings are discussed in the subsequent chapters.

III. CROSS-SECTIONS

A basic input into the microscopic transport models are the particle species and -energy dependent cross-sections of hadron-hadron interactions. The total cross-sections are interpreted geometrically. A collision between two hadrons will occur if $d < \sqrt{\sigma_{\text{tot}}/\pi}$, where d and σ_{tot} are the impact parameter of the hadrons and the total cross-section of the two hadrons, respectively. In the UrQMD model the total cross-section σ_{tot} depends on the isospins of colliding particles, their flavor and the c.m. energy. However, partial cross-sections are then used to calculate the relative weights for the different channels. Only a small fraction of all possible hadronic cross-sections has been measured. In the following sections, we compare the UrQMD cross-sections with experimental data. If no data are available, the additive quark model and detailed balance arguments are used to extrapolate such unknown observables.

A. Baryon-Baryon Cross-Sections

The total BB cross-section of the reaction $A + C \rightarrow D + E$ has the general form

$$\sigma_{\text{tot}}^{BB}(\sqrt{s}) \propto (2S_D + 1)(2S_E + 1) \frac{\langle p_{D,E} \rangle}{\langle p_{A,C} \rangle} \frac{1}{s} |\mathcal{M}|^2 \quad , \quad (3)$$

with the spins of the particles, S_i , momenta of the pairs of particles, $\langle p_{i,j} \rangle$, in the two-particle rest frame, and the matrix element $|\mathcal{M}|^2$. The matrix element $|\mathcal{M}|^2$, however, can take on a very complicated form and may be in general a function of all the particle's quantum numbers as well as its momenta and the c.m. energy.

If high quality experimental data on the respective cross section exists, a phenomenological fit to the respective data is by far the most accurate approach for implementing the cross section. Otherwise, we have to rely on simplified assumption for the matrix element and employ general symmetries, like the principle of detailed balance (see section IV A).

Let us start by investigating the total cross-section of proton-proton collisions from a beam momentum of 0.1 GeV/c up to 10^4 GeV/c as shown in Fig. 3. The total and inelastic cross-sections of the pp reaction are well measured in this energy region [15]. One finds a complex structure in this cross-section: local minima at 700 MeV/c ($E_{cm} \approx 2$ GeV) and 100 GeV/c ($E_{cm} \approx 10$ GeV), the maximum at 2 GeV/c ($E_{cm} \approx 2 - 3$ GeV) and a rise above 100 GeV/c. Note that the steep rise in the data below 300 MeV/c is due to soft Coulomb interaction of the protons and is taken care of via the potential interaction.

The structure in the pp cross-section is mainly due to the inelastic channels which are shown in Fig. 4. One clearly sees the Δ excitation with its increasing cross-section at low energies. The different partial cross sections depicted in Fig. 4 are discussed in section IV A.

A detailed comparison of prominent outgoing channels is depicted in Fig. 5. Here we show calculations of exclusive ($pp \rightarrow mpp$) and inclusive ($pp \rightarrow mX$) cross sections for the production of neutral mesons $m = \pi^0, \eta, \rho^0, \omega$ as a function of the excess energies $\epsilon = \sqrt{s} - \sqrt{s_{th}}$. Here $\sqrt{s_{th}}$ is the energy of the production threshold calculated as $\sqrt{s_{th}} = 2m_p + m_m$ with the proton mass m_p and the pole mass of the meson m_m . In the case of ρ^0 mesons we count only those with masses within ± 100 MeV around the pole mass to compare with data. The exclusive η production just above threshold [16] is overestimated by a factor of about two. Note that above 3.5 GeV the exclusive cross sections become less important because the string and multiple decay channels open and allow for multiple resonance production. For upcoming GSI-SIS experiments relevant \sqrt{s} values are below 4 GeV, where so far no data on the inclusive channels are available and therefore rely heavily on extrapolations.

In Fig. 6 the cross section of $pp \rightarrow \bar{p} + X$ reactions is shown. Good agreement with the data [57] is found over a large energy range.

At higher energies, the contributions of the different nucleonic resonances decrease and give way to the excitation of color strings, which is the dominant process at high energies in our model. The total cross section above the resonance region is given by the CERN-HERA parameterization [15] as shown in Table II.

Partonic pQCD scattering is not included into the UrQMD model in the present version. The difference between the total and the elastic cross-section is taken as the inelastic cross-section.

B. Meson-Baryon Cross-Sections

The MB cross-sections are dominated by the formation of s -channel resonances, i.e. the formation of a transient state of mass $m = \sqrt{s_{hh}}$, containing the total c.m. energy of the two incoming hadrons. On the quark level such a process implies that a quark from the

baryon annihilates an antiquark from the incoming meson. Below 2.2 GeV c.m. energy intermediate resonance states get excited. The total cross-section of these reactions are given by the expression:

$$\sigma_{tot}^{MB}(\sqrt{s}) = \sum_{R=\Delta, N^*} \langle j_B, m_B, j_M, m_M || J_R, M_R \rangle \frac{2S_R + 1}{(2S_B + 1)(2S_M + 1)} \times \frac{\pi}{p_{cm}^2} \frac{\Gamma_{R \rightarrow MB} \Gamma_{tot}}{(M_R - \sqrt{s})^2 + \Gamma_{tot}^2/4} \quad , \quad (4)$$

which depends on the total decay width Γ_{tot} , on the partial decay width $\Gamma_{R \rightarrow MB}$ and on the c.m. energy \sqrt{s} . At higher energies the quark-antiquark annihilation processes become less important. There, t -channel excitations of the hadrons dominate, where the exchange of mesons and Pomeron exchange determines the total cross-section of the MB interaction [17].

Figures 7 and 8 show the cross-section of pion-proton reactions at different energies. In Fig. 7 ($\pi^+ + p$) one probes predominantly the creation of the Δ^{++} (Δ^{*++}) resonance. Note that the low energy s -wave πp scattering is not included into the UrQMD fit. The resonance peak at $p = 1.5$ GeV/c is from the $\Delta(1900 - 1950)$ resonances. In comparison Fig. 8 ($\pi^- + p$) depicts many strong uncharged non-strange baryon resonances, e.g. the $\Delta^0(1232), \Delta^{0*}(1620), \dots, N^*(1535)$, etc. The total cross-section in the intermediate energy regime is therefore the sum of the individual excitation modes of baryon resonances, the s -wave at lower energies is left out.

Let us now investigate collisions of strange mesons with baryons. For $\bar{q}s$ mesons strange s -channel resonances can be formed on non-strange baryons due to the annihilation of the \bar{q} -quark. A comparison of these processes from UrQMD with the experimental data is shown in Fig. 9. The formation of hyperon resonances is clearly visible at lower energies, while the universal t -channel reaction dominates the high energy tail. Fig. 10 shows the cross-section of K^+ -mesons ($u\bar{s}$) on protons. In this case, the formation of resonances is forbidden, since the \bar{s} -quark cannot be annihilated by non-strange baryons (For strange baryons the formation of resonances is still possible). Here we use only the elastic channel and the t -channel excitation of both particles. The cross section at very high energies is given by the CERN-HERA parametrization as shown in Table II.

C. Meson-Meson Cross Sections

Due to the fact that the experimental preparation of meson beams and targets is restricted to π 's and K 's, only very little is known about MM collisions in general. For the description of heavy ion collisions the importance of this channel increases with energy: at 1 A GeV beam energy we find that the production of new hadrons (mostly pions) is only a ten percent effect. At AGS energies (10 A GeV) the amount of mesons roughly equals the number of incoming nucleons. Going on to the SPS (160 A GeV) the picture changes drastically: The produced particles dominate the reactions, while the incoming nucleons have dropped to a 15% admixture in particle density and multiplicity [18].

To describe the total meson-meson reaction cross-sections, we make use of the additive quark model (see below) and the principle of detailed balance, which assumes the reversibility of the particle interactions.

Fig. 11 compares the calculated cross-section of $\pi^+\pi^-$ scattering to experimental data [19]. The spectrum is dominated by the formation of the ρ with a mass of 770 MeV, the other two small peaks belong to the $f_0(970)$ and $f_2(1270)$ resonances. The $f_0(970)$ resonance is not visible in the data since the experimental analysis of meson-meson scattering is model dependent.

Figure 12 shows the implemented elastic $\pi^+\pi^+$ cross-section, which remains constant in the whole energy range where data are available [20,21].

Strangeness production in the meson-meson channel is possible, e.g. via the reaction $\pi^+\pi^- \rightarrow K\bar{K}$ as shown in Fig. 13.

Rescattering of strange mesons is implemented via the resonance formation (cf. Fig. 14 dominated by the K^* resonance [22]), or elastically as depicted in Fig. 15 [23].

Finally, we predict the cross-sections of $\pi^+\pi^0$, $\pi^+\rho^0$ and $\pi^+\eta$ -reactions (Fig. 16) which are of utmost importance for the production of thermal photons and dileptons. At higher energies other meson resonances can be formed. To model MM interactions above the resonance region $\sqrt{s} > 1.7$ GeV we use the rescaled total πp cross section:

$$\sigma_{\text{tot}}^{MM}(\sqrt{s} > 1.7 \text{ GeV}) = \sigma_{\text{tot}}^{\pi p}(\sqrt{s}) \frac{\sigma_{\text{AQM}}^{MM}}{\sigma_{\text{AQM}}^{\pi p}} . \quad (5)$$

This is justified, since at high energies the total cross section is given by quark counting. In the energy region from $\sqrt{s} > 1.7$ GeV to $\sqrt{s} < 6$ GeV s -channel interactions are taken into account, while from $\sqrt{s} > 3$ GeV on t -channel excitation of both mesons becomes the MM interaction process of increasing importance in the model.

The cross section for high energetic reactions are taken from the AQM-rescaled π^+p parametrization by the CERN-HERA group (see Table II).

D. Antibaryon–Baryon Cross-Sections

The physics of baryon–antibaryon interactions has been an area of much theoretical and experimental activity for a rather long period. It is well-known that at energies $p_{\text{lab}} \leq 100 \text{ GeV}/c$ an important contribution to the total interaction cross-section comes from the process of annihilation, where only mesons are left in the final state. Though the earlier experiments on $\bar{p}p$ –annihilation revealed a number of differences from the non-annihilation channels, it is not clearly understood whether these differences arose simply due to the kinematic restrictions on the available phase space, or whether they are related to dynamical differences between the non-annihilation and annihilation mechanisms. The experimental results obtained in [24] by comparison of pp with non-annihilation $\bar{p}p$ interactions at 32 GeV/c support the conclusion of equivalence of pp and non-annihilation $\bar{p}p$ interaction processes.

Still, the nature of the baryon annihilation is subject to theoretical discussions. In the framework of the quark models based on topological $1/N$ expansion, the annihilation process is associated with the annihilation of string junctions, i.e. the point where strings are connected, such that the baryons have a Y -form. In this case three $q\bar{q}$ strings are formed. The theory also allows for diagrams where the string junctions and one or two of the valence quarks can annihilate, corresponding to the formation of two strings or one string. Other

theories consider an annihilation mechanism without invoking the string junction hypothesis. This intriguing question has yet to be clarified (for review see, e.g. [25], and references herein).

To avoid the difficulties attributed to these theoretical approaches, UrQMD is adjusted to known experimental data. The total $\bar{p}p$ cross-section is shown in Fig. 17, as well as the annihilation and the elastic cross-sections. The UrQMD parameterizations depicted by lines are taken from Koch and Dover [26]:

$$\sigma_{\text{ann}}^{\bar{p}p} = \sigma_0^N \frac{s_0}{s} \left[\frac{A^2 s_0}{(s - s_0)^2 + A^2 s_0} + B \right] , \quad (6)$$

with $\sigma_0^N = 120$ mb, $s_0 = 4m_N^2$, $A = 50$ MeV and $B = 0.6$. The $\bar{n}p$ cross-section does not differ significantly from the $\bar{p}p$ cross-section [27], hence they are set equal in the UrQMD model.

At higher energies, CERN-HERA parameterizations [15] are used for the total and elastic channel:

$$\sigma_{\text{tot,el}}^{\bar{p}p}(p) = A + B p^n + C \ln^2(p) + D \ln(p) , \quad (7)$$

with the laboratory momentum p in GeV/ c and the cross-section σ in mb. The parameters of the fit are listed in Table II.

Below $p_{\text{tab}} < 5$ GeV/ c the following parameterization is used:

$$\sigma_{\text{tot}}(p) = \begin{cases} 75.0 + 43.1p^{-1} + 2.6p^{-2} - 3.9p & ; \quad 0.3 < p < 5 \\ 271.6 \exp(-1.1p^2) & ; \quad p < 0.3 \end{cases} \quad (8)$$

$$\sigma_{\text{el}}(p) = \begin{cases} 31.6 + 18.3p^{-1} - 1.1p^{-2} - 3.8p & ; \quad 0.3 < p < 5 \\ 78.6 & ; \quad p < 0.3 \end{cases} \quad (9)$$

The sum of annihilation and elastic cross-sections do not yield the total cross-section:

$$\Delta\sigma = \sigma_{\text{tot}} - \sigma_{\text{el}} - \sigma_{\text{ann}} \quad (10)$$

In UrQMD this difference $\Delta\sigma$ is interpreted as the diffractive cross-section which describes the excitation at least one of the collision particles to a resonance or to a string via Pomeron exchange.

The annihilation of baryon–antibaryon pairs proceeds in the UrQMD model according to *rearrangement* diagrams. Here the formation of two $q\bar{q}$ -strings of equal energies in the c.m. system is assumed while the remaining constituent quarks are rearranged into newly produced hadrons. The generalization of the $\bar{p}p$ cross-section towards all possible antibaryon–baryon collisions can be done in different ways:

1. The anti-baryon baryon cross-section at a given c.m. energy \sqrt{s} is equal to the $\bar{p}p$ annihilation cross-section at the same \sqrt{s} :

$$\sigma_{\bar{B}B}|_{\sqrt{s}} = \sigma_{\bar{p}p}|_{\sqrt{s}} \quad (11)$$

2. The anti-baryon baryon cross-section at a given relative momentum p_{rel} is equal to the $\bar{p}p$ annihilation cross-section at the same p_{rel} (Fig. 18):

$$\sigma_{\bar{B}B}|_{p_{rel}} = \sigma_{\bar{p}p}|_{p_{rel}} \quad (12)$$

In the UrQMD we have chosen the first parameterization. Since $\sigma_{\text{ann}} \propto s^{-1/2}$, the annihilation cross-section drops rapidly with rising particle mass. The different treatment this cross-section can lead to systematic shifts in the antibaryon distributions for massive systems. Therefore, anti-baryon production off nuclei may be used to solve this ambiguity.

E. The Additive Quark Model (AQM)

Unknown cross-sections are calculated on the basis of the Additive Quark Model (AQM) [28,29], which assumes the existence of dressed valence quarks, interacting very weakly inside of the hadron. At the phenomenological level, the AQM gives a correct quantitative and qualitative description of, e.g., the asymmetry of c.m. spectra of secondaries in meson–nucleon and photon–nucleon reactions. The AQM has predicted also the important role of resonances for the multiple production of particles in hadronic interactions. To apply the AQM to calculations of heavy ion reactions, one needs to know the cross-sections of the quark interactions, which can be evaluated from the quark masses. Then, the unknown total cross-section of the high energy reaction can be calculated assuming a 40% reduced s -quark cross-section (compared to that of u - and d -quark). The elastic cross-section is derived from Regge theory [30]:

$$\sigma_{\text{elastic}} = 0.039\sigma_{\text{total}}^{\frac{3}{2}} \text{ [mb]} \quad , \quad (13)$$

where

$$\sigma_{\text{total}} = 40 \left(\frac{2}{3}\right)^{m_1+m_2} \left(1 - 0.4\frac{s_1}{3-m_1}\right) \left(1 - 0.4\frac{s_2}{3-m_2}\right) \text{ [mb]} \quad , \quad (14)$$

where $m_i = 1(0)$ for particle i being a meson (a baryon) and s_i is the number of strange quarks in particle i . This formula results from the high energy reactions, therefore there is no difference between antiparticles and particles. For BB-reactions no additional energy dependence is employed in collisions involving strange baryons. Non-strange baryon cross-sections are not treated via the Additive Quark Model, they have an explicit energy dependence in line with experimental data. The MB and MM cross-sections are rescaled via:

$$\sigma_{X_1X_2}(\sqrt{s}) = \frac{\sigma_{\pi N}(\sqrt{s})}{\sigma_{\pi N}^{\text{AQM}}} \sigma_{X_1X_2}^{\text{AQM}} \quad . \quad (15)$$

The hyperon-nucleon cross-section, which is taken in the UrQMD model from the Additive Quark Model, is in good agreement with the data above $p_{\text{lab}} = 300$ MeV (cf. Fig. 19). The total cross-sections calculated for baryon-baryon, meson-baryon and meson-meson interactions are listed in Tables III–V.

F. Color Fluctuations, Color Opacity and Color Transparency

Quantum chromodynamics has important applications of the dynamical role of color degrees of freedom to the strong interactions at ultrarelativistic energies (for a review, see [31,32] and references therein). The theory is presented in Ref. [31] in detail, here we just sketch the main ideas of color optics and coherent phenomena in high energy physics. Hadrons are dynamical objects which come in Fock space of configurations of very different spatial sizes. At high energies, incident hadronic quark–gluon configurations can be considered frozen as a result of Lorentz time dilation. Due to the long coherence length at such high energies one can apply geometrical color optics. Small objects produced in hard processes with high momentum transfer Q^2 then have reduced interaction cross sections. In processes with moderate Q^2 such compact objects, which are a coherent superposition of eigenstates of the QCD Hamiltonian, should gain size. When the quark–gluon configuration is large, it will lead to an increased interaction cross-section of the hadron with the nuclear medium.

Therefore, the fluctuations of the hadron’s spatial extent give rise to the color transparency and color opacity phenomena: When a small object is produced, it interacts only very weakly with other hadrons due to color screening. Moreover, since - at sufficiently high energies - the small-sized configuration of this object is frozen, the nuclear medium appears to be transparent for such hadrons (color transparency). In contrast, hadronic configurations which are larger than average interact with larger cross-section, giving rise to color opacity.

Nucleus-nucleus collisions provide a tool to investigate the effect of color transparency, for instance, in the production of leading nucleons. On the other hand, the complementary color opacity effect, i.e. large-sized configurations, can cause stronger stopping and significant fluctuations in the transverse energy of secondaries in central reactions.

A first step to investigate these QCD effects within a microscopic transport model is made by incorporating the color fluctuations in the elementary hadron–hadron reactions in the UrQMD model. Thus, one needs to know the probability $P(\sigma)$ that a given configuration interacts with a nucleon with a total cross-section σ . It is convenient to consider moments of the distribution:

$$\langle \sigma^0 \rangle = \int d\sigma \bar{\sigma}^0 P(\sigma) = 1 \quad , \quad (16)$$

$$\langle \sigma^1 \rangle = \int d\sigma \bar{\sigma}^1 P(\sigma) = \bar{\sigma} \quad , \text{etc.} \quad , \quad (17)$$

where $\bar{\sigma}$ denotes the average cross-section. The second moment $\langle \sigma^2 \rangle$ can be determined from the diffractive dissociation experiments. In addition, further information can be obtained from QCD, which implies [31]:

$$P(\sigma) \propto \sigma^{N_q-2} \quad , \quad (18)$$

for $\sigma \rightarrow 0$, where N_q is the number of valence quarks. Thus, for the nucleon and the pion distributions it follows for $\sigma \rightarrow 0$:

$$P_N(\sigma) \propto \sigma \quad , \quad (19)$$

$$P_\pi(\sigma) \propto \text{constant} \quad . \quad (20)$$

From these arguments, $P(\sigma)$ can be constructed. Fig. 20 shows the resulting broad $P(\sigma)$ distribution for proton projectiles and the even broader one for the pions [31].

The effect of the color fluctuations on proton-proton interactions at different impact parameters, b , is shown in Fig. 21 for the UrQMD model. The charged pion multiplicity distribution decreases monotonically with rising b . $N_\pi(b)$ has a non-vanishing tail for $b \geq 1.1$ fm, in contrast to the abrupt geometrical edge of the distribution as calculated in the static geometric models without color fluctuations.

IV. THE REACTION CHANNELS

A. Resonances

The production and decay of resonances is the most important h-h reaction channel below $\sqrt{s} = 5$ GeV for BB and 3 GeV for MM and MB reactions. Baryon resonances are produced in two different ways, namely

i) *hard production*: $N+N \rightarrow \Delta N, \Delta\Delta, N^*N$, etc.

ii) *soft production*: $\pi^- + p \rightarrow \Delta^0, K^- + p \rightarrow \Lambda^* \dots$

The formation of s -channel resonances is fitted to measured data, e.g. in the reaction $A + C \rightarrow D + E$ we use the general form

$$\sigma_{tot}^{BB}(\sqrt{s}) \propto (2S_D + 1)(2S_E + 1) \frac{\langle p_{D,E} \rangle}{\langle p_{A,C} \rangle} \frac{1}{s} |\mathcal{M}(m_D, m_E)|^2, \quad (21)$$

with the spins of the particles, S_i , momenta of the pairs of particles, $\langle p_{i,j} \rangle$, in the two-particle rest frame, and the matrix element $|\mathcal{M}(m_D, m_E)|^2$, which here depends only on the masses of the outgoing hadrons, m_i .

There are six channels of the excitation of non-strange resonances in the UrQMD model, namely $NN \rightarrow N\Delta_{1232}, NN^*, N\Delta^*, \Delta_{1232}\Delta_{1232}, \Delta_{1232}N^*$, and $\Delta_{1232}\Delta^*$. The Δ_{1232} is explicitly listed, whereas higher excitations of the Δ resonance have been denoted as Δ^* . For each of these 6 channels specific assumptions are made with respect to the form of the matrix element \mathcal{M} , and the free parameters are adjusted to the available experimental data, when available:

1. $NN \rightarrow N\Delta_{1232}$ excitation:

$$|\mathcal{M}(\sqrt{s}, m_3, m_4)|^2 = A \frac{m_\Delta^2 \Gamma_\Delta^2}{((\sqrt{s})^2 - m_\Delta^2)^2 + m_\Delta^2 \Gamma_\Delta^2}, \quad (22)$$

with $m_\Delta = 1.232$ GeV, $\Gamma_\Delta = 0.115$ GeV and $A = 40000$. Note that this form of the matrix element has been adjusted to fit the data shown in figure 22.

2. $NN \rightarrow NN^*, NN \rightarrow N\Delta^*, NN \rightarrow \Delta_{1232}N^*$ and $NN \rightarrow \Delta_{1232}\Delta^*$ excitation:

$$|\mathcal{M}(m_3, m_4)|^2 = A \frac{1}{(m_4 - m_3)^2 (m_4 + m_3)^2}, \quad (23)$$

with $A = 6.3$ for $NN \rightarrow NN^*$, $A = 12$ for $NN \rightarrow N\Delta^*$ and $A = 3.5$ for $NN \rightarrow \Delta_{1232}N^*$. In the case of $NN \rightarrow \Delta_{1232}\Delta^*$ there are insufficient data available, therefore we use the same matrix element and parameters as in the case of $NN \rightarrow \Delta_{1232}N^*$. Since $m_3 \neq m_4$ is valid for all above cases, the matrix element cannot diverge.

3. $NN \rightarrow \Delta\Delta$ excitation:

$$|\mathcal{M}(m_3, m_4)|^2 = A \quad , \quad (24)$$

with $A = 2.8$.

Figure 22 shows the fit of the UrQMD $pp \rightarrow N\Delta_{1232}$ cross section to experimental measurements [56]. The measurements refer to the $\Delta^+ + n$ exit channel and have been rescaled to match the full isospin-summed cross section. In the case of the exclusive Δ_{1232} cross section the quality of the data and thus also the quality of the resulting fit is very good. For higher resonance excitations this is unfortunately no longer the case and additional measurements are needed to clarify the situation. One has to keep in mind, however, that the experimental extraction of exclusive resonance production cross sections is only possible via two- or three-particle correlations (e.g. a pion-nucleon correlation in the case of the Δ) which introduces large systematic errors, especially for broad resonances.

In figure 23 the UrQMD cross sections for the processes $pp \rightarrow pp_{1440}^*$, $pp \rightarrow pp_{1520}^*$, $pp \rightarrow pp_{1680}^*$ and $pp \rightarrow pp_{1700}^*$ are compared to data [56]. One single parameter has been used to fit all four cross sections. The data situation is not as good as in the case of the Δ_{1232} resonance, some ambiguities are visible which results in the quality of the fit being not as good as in the previous case. The parameters for the other classes are fitted in the same fashion.

The cross section for exclusive $\Delta_{1232}\Delta_{1232}$ can be seen in figure 24. The data points [56] hint at a resonance like structure which cannot be reproduced with the UrQMD ansatz for resonance-excitation cross sections. However, the data deviates considerably from other cross sections for resonance excitation (e.g. $NN \rightarrow N^*\Delta^*$). Considering hadron-universality and the similarities in all other resonance excitation cross sections this casts a certain doubt on the accuracy of the measurement of the resonance-like peak.

Figure 25 shows the UrQMD fit for the exclusive Δ_{1920}^*N production. The same matrix element is used for the entire class of $NN \rightarrow \Delta^*N$ reactions. In the case of exclusive Δ^*N^* production the matrix element has been fitted to the $\Delta_{1232}^*N_{1680}^*$ exit channel (see figure 26). The extrapolation to the case of $\Delta_{1232}^*N_{1520}^*$ production can be seen in figure 27. For the exclusive $pp \rightarrow \Delta\Delta^*$ reaction class the data situation is unsatisfactory, therefore we used the same matrix-element as in the $pp \rightarrow N\Delta^*$ case.

The decay of the resonances proceeds according to the branching ratios compiled by the Particle Data Group [15]. The resonance decay products have isotropical distributions in the rest frame of the resonance. If the resonance decays into $N > 2$ particles, then the corresponding N -body phase space is used to calculate their N momenta stochastically. It is necessary to note that a consistent description of angular momentum distributions points to a rather intricate problem of transport theory itself: If one considers the whole scattering interaction to be described by one single quantum mechanical process there are correlations between the final and the initial stage. For instance the angular distribution of the final

particles with respect to the axes of the incoming momenta in the CMS system. However, a fitting of the angular distributions to experimental data may conflict with the basic assumption of transport theories that the multiple scattering processes can be considered to be of Markovian type, i.e. after each scattering process or resonance formation the outgoing particles completely forget about their entrance channels. In the case of a spin 0 resonance there is no preferred direction for the emission of the final particles, while for spin 1 (and other) the different magnetic quantum numbers are statistically occupied, so that also in these cases there is no preferred angle of emission¹.

All produced particles are able to rescatter within the nuclear medium, therefore the excitation of resonances by the annihilation of mesons on baryons included as depicted in Fig. 7 for the reaction $\pi^+ + p \rightarrow \Delta^{++(*)}$.

Also the $\pi^- + p$ channel (Fig. 8) shows a rich structure of baryon resonances. The total meson-baryon cross section is given by formula 4. There, the total and partial decay widths also define the inverse reaction, i.e. the different decay-channels of the respective resonance. Thus, the principle of detailed balance is applied. Based on this principle we calculate all resonance formation cross sections from the measured decay properties of the possible resonances up to c.m. energies of 2.25 GeV/ c^2 for baryon resonance and 1.7 GeV/ c^2 in the case of MM and MB reactions. Above this energy collisions are modeled by the formation of s -channel string or, at higher energies (beginning at $\sqrt{s} = 3$ GeV), by one/two t -channel strings. In the strangeness channel elastic collisions are possible for those meson-baryon combinations which are not able to form a resonance, while the creation of t -channel strings is always possible at sufficiently large energies (c.f. Fig. 9 for the formation of hyperon resonances and Fig. 10 for the non-resonant channel). At high collision energies both cross section become equal due to quark counting rules.

In more general terms, the principle of detailed balance can be derived by assuming time-reversal invariance of the interaction Hamiltonian and can be formulated in the following way:

$$\sigma(y \rightarrow x) p_y^2 g_y = \sigma(x \rightarrow y) p_x^2 g_x \quad , \quad (25)$$

with \vec{p} denoting the c.m.-momenta of the particles and g being the spin-isospin degeneracy factors. Thus, if the cross section of the reaction $x \rightarrow y$ is known, the back reaction $y \rightarrow x$ can be easily obtained. This principle is in UrQMD widely applied for the calculation of baryon-resonance absorption cross sections, such as $\Delta(1232) + N \rightarrow N + N$. For a detailed discussion of the application of the principle of detailed balance to resonance absorption and \sqrt{s} -dependent decay widths we refer to [5].

As was mentioned above, not only baryon-baryon and meson-baryon collisions have to be included in the proposed scheme. At high energies and in massive AA systems meson-meson collisions may dominate the multiple production of secondaries. Unfortunately, there are only few channels for which the experimental information exists, like the process of $\pi^+ \pi^-$ scattering (Fig. 11), which is fairly described by the UrQMD model.

¹For a detailed discussion of the influence of non-markovian processes in the transport theory of heavy ion collisions we refer the reader to Refs. [33,34].

B. Strings

Both, for the high energy regime and for baryon–antibaryon annihilation we apply a string model (similar to the LUND model [35]) to describe the inelastic reactions. The constituents, quark and diquark (or anti-quarks), of the incoming hadron also define the predominant emission patterns of the events. The amount of stopping in nucleus-nucleus is strongly correlated to the detailed dynamics of the diquark in the hadronic medium [5]. Recently different additional mechanisms of baryon number transport in nucleus-nucleus reactions have been investigated: Baryonic junctions as suggested by [36] which yield an enhanced hyperon and proton production cross section at central rapidities [37]; di-quark breaking due to interaction with the hadronic medium as predicted by [38]. The di-quark breaking component is also taken into account in the UrQMD model (di-quark breaking probability= 10%). However, the above mechanisms are of minor importance in the UrQMD approach since rescattering of the leading di-quark with hadrons is explicitly taken into account.

Since gluons are massless particles with spin $J = 1$, the static strong interaction between quarks at small distances ($r \ll 1/\Lambda_{\text{QCD}}$) may be described by a potential $V_0 \propto -\alpha_S/r$. At sufficiently large distances the color field between two quarks or anti-quarks transforms into the color string. Denoting the string tension as κ one defines the linear string potential

$$V_1 = \kappa |z_1 - z_2| \quad , \quad (26)$$

between the quarks/diquarks located at z_1 and z_2 , respectively. This form of the potential is chosen from heuristic considerations, based on the quark confinement hypothesis, and is supported by lattice QCD calculations [40].

The transverse directions have not to be taken into account, since they are negligibly small compared to the longitudinal excitation of the hadron string. Hence, we get the dynamics of the quark system (with quark momenta p_1 and p_2) from the Hamiltonian H

$$H = |p_1| + |p_2| + \kappa |z_1 - z_2| \quad , \quad (27)$$

which leads to the following equations of motion for the massless endpoints of the string:

$$\frac{dp_i}{dt} = -\frac{\partial H}{\partial z_i} = -\text{sign}(z_i - z'_i) \kappa \quad , \quad (28)$$

$$\frac{dz_i}{dt} = +\frac{\partial H}{\partial p_i} = \text{sign}(p_i) \quad . \quad (29)$$

A change in momentum is directly related to the sign of $(z_i - z'_i)$, while the direction of propagation is defined by the sign of the momentum p_i of the quark. This results in a typical "yo-yo" type evolution of the quark system.

If the momentum transfer is large enough, the excitation of the string may exceed some critical limit. After that it will be energetically favorable to break the string into pieces by producing $q\bar{q}$ -pairs from the vacuum. Each of the produced $q\bar{q}$ -pairs will have small relative momenta in their rest frame. Owing to the fact that the color string is uniformly stretched, the hadrons produced as a result of the string fragmentation will be uniformly distributed within the kinematically allowed interval between $y_{\min} = 0$ and $y_{\max} = \ln(s/m_T^2)$.

The probability of the pair production process has been calculated by Schwinger for the case of an infinite homogeneous electrical field. His result can be used to motivate the decay of QCD color field between the quarks. Note that QCD is a non-abelian theory, therefore the color field need not be homogeneous and it is definitely not infinite. This leads to the modifications of string decays which will be discussed later.

The probability $|M|^2$ for the creation of a quark-antiquark pair with mass m in a color field with a string tension κ is:

$$|M|^2 = \text{constant} \times \exp\left(-\frac{\pi m^2}{\kappa}\right) \quad , \quad (30)$$

where a typical value for κ is 1 GeV/fm. This relation is motivated by Schwinger's QED-based result for particle-antiparticle creation in a strong electric field (see the discussion of formula 38 in section IV B 1). The relative production probabilities of the different quark flavors are adjusted to e^+e^- -data:

$$u : d : s : \text{diquark} = 1 : 1 : 0.35 : 0.1 \quad . \quad (31)$$

The production of charmed (and heavier) quarks is strongly suppressed in the string picture, hence they are exclusively produced in hard QCD processes. The elementary diquark is introduced to allow for baryon-antibaryon production in the string. A schematic view of the decaying string is shown in Fig. 28 – a non-strange baryon decays into a hyperon, a kaon and a pion.

To decide which type of hadron is produced from the quark configuration that is created in the color field we choose in the case of a produced

- (i) *baryon* – the octet and decuplet with equal probabilities;
- (ii) *meson* – the meson nonet with a probability proportional to the spin degeneracy and inverse mean mass m ,

$$P_{\text{multiplet}} \propto \frac{2S + 1}{\langle m \rangle_{\text{multiplet}}} \quad . \quad (32)$$

The singlet states are mixtures of $u\bar{u}$, $d\bar{d}$ and $s\bar{s}$. They are projected onto SU(3) hadrons with the flavor mixing angles from the quadratic Gell-Mann-Okubo mass formula [39]. For the scalar mesons this formula is not applicable, here an ideal mixing angle ($\tan(\theta) = 1/\sqrt{2}$) is assumed (The mixing angles are depicted in Table VI).

The Field–Feynman fragmentation mechanism [41], which allows the independent string decay from both ends of the string is used in the UrQMD model. The string break-up is treated iteratively: String \rightarrow hadron + smaller string. The conservation laws are fulfilled. The diquark is permitted to convert into mesons via the breaking of the diquark link, thus transporting the baryon number into central rapidities.

On both sides of the fragmenting string the new particles are formed randomly. If a resonance is produced, its mass is determined by a Breit-Wigner mass distribution. The transverse momentum is assigned to this particle according to a thermal momentum distribution, resulting in a temperature of 170 MeV. After that the fragmentation function determines the fraction of the longitudinal momentum of the string transferred to the hadron. This procedure can be described in a covariant manner by the light cone variables defined as:

$$z^\pm = t \pm z \quad \text{and} \quad p^\pm = E \pm p \quad . \quad (33)$$

The light cone momentum p_{hadron}^\pm given to the newly produced hadron is:

$$p_{\text{hadron}}^\pm = z_{\text{fraction}}^\pm p_{\text{total}}^\pm \quad (34)$$

The fragmentation of a baryonic string reads:

$$p^- \underbrace{(qqq\bar{q})}_{\text{String}} = z_{\text{fraction}}^- p^- \underbrace{(qqq)}_{\text{Baryon}} + (p^- - z_{\text{fraction}}^- p^-) \underbrace{\bar{q}q}_{\text{String}} \quad . \quad (35)$$

The main input is the fragmentation function which yields the probability distribution $p(z_{\text{fraction}}^\pm, m_t)$. This function regulates the fraction of energy and momentum given to the produced hadron in the stochastic fragmentation of the color string. For newly produced particles the Field-Feynman function [41]:

$$p(z_{\text{fraction}}^\pm) = \text{constant} \times (1 - z_{\text{fraction}}^\pm)^2, \quad (36)$$

is used. $P(z)$ drops rapidly with increasing z (Fig. 29). Therefore, the longitudinal momenta of e.g. produced antibaryons (Fig. 30) and pions (Fig. 31) are small (they stick to central rapidities), in line with the experimental data. The rapidity spectra of these particles have a characteristic Gaussian-like shape, in contrast to the baryon spectra in pp, as it is clearly seen in Figure 30.

The proton is on average less stopped, since it is build up from the leading diquark in the string (leading particle effect). Fig. 32 compares the x_F distribution of protons and Λ 's for the Feynman scaling variable $x_F = 2p_{\parallel}/\sqrt{s}$ measured in pp reactions at 205 GeV/c. The data on leading baryons can only be reproduced when a modified fragmentation function is used for the leading baryons (cf. Fig. 29, dashed curve). This leading baryon fragmentation function is of Gaussian form:

$$p(z_{\text{fraction}}^\pm) = \text{constant} \times \exp \left[-\frac{(z_{\text{fraction}}^\pm - b)^2}{2a^2} \right] \quad , \quad (37)$$

with parameters $a = 0.275$ and $b = 0.42$.

It is obvious that modeling the momentum loss in elementary collisions has a strong influence on the rapidity spectra of particles produced in heavy-ion collisions. This can be seen if one compares the spectra of p, Λ 's (created from the leading baryon) and $\bar{\Lambda}$'s or mesons (created from newly produced quarks) in lead-lead collisions at the SPS energies [5].

1. Finite Size Effects

Let us now discuss finite size effects in the process of string fragmentation. The string is essentially a color field which connects two color charges, the [3] quark and the $[\bar{3}]$ diquark or anti-quark, at the ends of the string. Quantum electrodynamics (QED) predicts spontaneous particle–antiparticle creation in strong electric fields [42,43]. This effect should hold for particle creation in a strong color fields. Schwinger's QED result

$$W_\infty = \frac{(eE)^2}{4\pi^3} \sum_{N=1}^{\infty} \frac{1}{N^2} \exp\left(-N\pi \frac{m^2}{eE}\right) \quad (38)$$

is often adopted to the case of color fields by equating $|eE|$ with the string tension κ .

However, for strings, several important assumptions, which lead to Schwinger's result are not fulfilled: Firstly, the color field is not infinitely extended. It is bound radially by the interaction length of the gluons and longitudinally roughly by the $[3]$ and $[\bar{3}]$ endpoints. Secondly, the two endpoints of the string move (with close to the speed of light) in opposite directions. Finally, the assumption of a constant field strength κ seems to be fulfilled along the string, but may become invalid in hot and dense matter [44].

The influence of the finite radial size of the string can be studied by solving the Dirac equation for the (newly produced) pairs in a finite volume. The field is restricted to a cylindrical volume of length L and area πR^2 , where R is the cylinder radius. Along the cylinder axis a homogeneous color field is assumed. The boundary condition on the surface of the cylinder leads to enclosure of the color charges. Taking $L \rightarrow \infty$ neglects the longitudinal direction.

The constraint on the cylinder surface is given by linear MIT-boundary conditions [45], thus we have to solve the equations:

$$(\gamma_\mu p^\mu - e\gamma_\mu A^\mu - m)\psi(x) = 0 \quad , \quad (39)$$

$$(in^\mu \gamma_\mu - 1)\psi(x) = 0 \quad (x \in \partial V) \quad . \quad (40)$$

The MIT model allows for an analytic solution [46]. The occupation numbers in the limits $t \rightarrow \pm\infty$ yield the pair creation probability as [46]

$$W_R = \frac{(eE)^2}{4\pi^3} \sum_{N=1}^{\infty} \frac{1}{N^2} \exp\left(-N\pi \frac{m^2}{eE}\right) \times \left\{ \frac{2\pi N}{eER^2} \sum_{n,\mu} \exp\left[-N\pi \frac{(k_{n\mu}R)^2}{eER^2}\right] \right\} \quad . \quad (41)$$

Thus the string radius is directly related to the pair creation rate W_R , with $k_{n\mu}$ being the n^{th} momentum eigenvector in the solution of Eqs. (39 and 40) for a given projection μ of the corresponding Bessel functions.

The expression in curly brackets gives the deviation from the Schwinger formula. For $R \rightarrow \infty$ this second factor vanishes and one is back to the infinite case. This result allows to calculate the strangeness suppression $f_s(R) = W_R(s)/W_R(u)$ for different string radii as shown in Fig. 33.

The overall pair creation rate has been calculated as a function of the longitudinal size of the color field for the corresponding Dirac equation [47] in terms of confluent hypergeometric functions. The resulting particle production rate per volume dV and time interval dt , $dN/(dV dt dp_T)$ at $p_T = 0$ is shown in Fig. 34 as a function of z , the distance from the string center, for different string lengths L . A clear depletion of particle production near the endpoints of the string endings is visible (Eq.38). For short strings the particle production gets enhanced toward the string center.

The above discussed finite size effects have a strong influence on the results, especially on the production of heavy quarks and particles like anti-baryons, -hyperons, etc. Up to now these corrections are included only in the non-strange antibaryon sector. This effect is very important especially in the case of the Λ -particle, since it is mostly created at the

string ends in the fragmentation of a leading proton. Indeed, it has been reported that most of the transport models which use a string fragmentation scheme based on the Schwinger formalism tend to overestimate the Λ 's [48]. Therefore, this finite size effects shall be included for strange baryons, in order to correct the overestimated number of Λ 's and $\bar{\Lambda}$'s.

V. THE GENERATION OF TRANSVERSE MOMENTUM

In hot and dense nuclear matter, most hadrons suffer interactions from the many surrounding particles. As a result, the effective mass may change with density. Many dynamical properties of hadrons are modified in the medium. In-medium two-body scattering cross-sections may differ from the free space values. Those effects can be studied in the framework of relativistic transport theory, i.e. the relativistic Boltzmann-Uehling-Uhlenbeck (RBUU) equation. This type of transport equation has been used extensively to the study of relativistic heavy-ion collisions and turned out to be very successful. The UrQMD approach uses an analytical expression for the differential cross-section of in-medium NN elastic scattering derived from the collision term of the RBUU equation [49] to determine the scattering angles between the outgoing particles in elementary hadron-hadron collisions. It is assumed that the angular distributions for all relevant two-body processes are similar modified in an analogous manner. They are approximated by the differential in-medium NN elastic scattering cross-section:

$$\sigma_{NN \rightarrow NN}(s, t) = \frac{1}{(2\pi)^2 s} [D(s, t) + E(s, t) + (s, t \longleftrightarrow u)], \quad (42)$$

with the direct term

$$\begin{aligned} D(s, t) = & \frac{(g_{NN}^\sigma)^4}{2(t - m_\sigma^2)^2} (t - 4m^{*2})^2 + \frac{(g_{NN}^\omega)^4}{(t - m_\omega^2)^2} (2s^2 + 2st + t^2 - 8m^{*2}s + 8m^{*4}) \\ & + \frac{24(g_{NN}^\pi)^4}{(t - m_\pi^2)^2} m^{*4} t^2 - \frac{4(g_{NN}^\sigma g_{NN}^\omega)^2}{(t - m_\sigma^2)(t - m_\omega^2)} (2s + t - 4m^{*2}) m^{*2}, \end{aligned} \quad (43)$$

and the exchange term

$$\begin{aligned} E(s, t) = & -\frac{(g_{NN}^\sigma)^4}{8(t - m_\sigma^2)(u - m_\sigma^2)} [t(t + s) + 4m^{*2}(s - t)] + \frac{(g_{NN}^\omega)^4}{2(t - m_\omega^2)(u - m_\omega^2)} (s - 2m^{*2}) \\ & \times (s - 6m^{*2}) - \frac{6(g_{NN}^\pi)^4}{(t - m_\pi^2)(u - m_\pi^2)} (4m^{*2} - s - t) m^{*4} t \\ & + (g_{NN}^\sigma g_{NN}^\pi)^2 \left[\frac{3m^{*2}(4m^{*2} - s - t)(4m^{*2} - t)}{2(t - m_\sigma^2)(u - m_\pi^2)} + \frac{3t(t + s)m^{*2}}{2(t - m_\pi^2)(u - m_\sigma^2)} \right] \\ & + (g_{NN}^\sigma g_{NN}^\omega)^2 \left[\frac{t^2 - 4m^{*2}s - 10m^{*2}t + 24m^{*4}}{4(t - m_\sigma^2)(u - m_\omega^2)} + \frac{(t + s)^2 - 2m^{*2}s + 2m^{*2}t}{4(t - m_\omega^2)(u - m_\sigma^2)} \right] \\ & + (g_{NN}^\omega g_{NN}^\pi)^2 \left[\frac{3m^{*2}(t + s - 4m^{*2})(t + s - 2m^{*2})}{(t - m_\omega^2)(u - m_\pi^2)} + \frac{3m^{*2}(t^2 - 2m^{*2}t)}{(t - m_\pi^2)(u - m_\omega^2)} \right], \end{aligned} \quad (44)$$

The (pseudo-)scalar and vector coupling constants are $g_{NN}^\pi = 1.434$, $g_{NN}^\sigma = 6.9$, and $g_{NN}^\omega = 7.54$ and m^* is the in-medium mass, s, t, u are the Mandelstam variables. The in-medium single-particle energy is given by

$$E^*(p) = \sqrt{\mathbf{p}^{*2} + m^{*2}} . \quad (45)$$

The formula for the differential cross section of in-medium NN elastic scattering can be used for elementary hadron-hadron collision if it is scaled by

$$s \rightarrow s - (m_1^* + m_2^*)^2 + 4m^{*2} , \quad (46)$$

where m_1^* and m_2^* denote the effective masses of the incoming hadrons. Furthermore, we take into account finite size effects of the hadrons and part of the short range correlation by introducing a phenomenological form factor at each vertex. For the baryon-baryon-meson vertex the common form

$$F_{BBM} = \frac{\Lambda_M^2}{\Lambda_M^2 - t} . \quad (47)$$

is used, where Λ_M is the cut-off mass for meson M .

The total energy and the masses of the incoming hadrons serve as input for calculating the angular distribution. It is worth to stress again that Eq.(42) is used to calculate only the angular distributions for all elementary elastic two-body processes but not the corresponding total cross sections. The inverse slopes ('temperatures') as calculated in the UrQMD from the transverse momentum spectra of pions - by fitting the $1/m_t dN/dm_t$ distribution with an exponential - compare well with values extracted from thermal fits to data² [50] (Fig. 35).

VI. PARTICLE YIELDS, LONGITUDINAL AND TRANSVERSE SPECTRA

The UrQMD model reproduces nicely the total, elastic and inelastic cross-sections of numerous hadronic reactions. The model also predicts the particle multiplicities (i.e. the inclusive cross-sections) as well as the (Lorentz-invariant) cross-sections, which may come in the form of x_F -, rapidity-, or transverse momentum distributions. The abundances of the most important particle species produced in pp collisions at 12 GeV/c [51] are listed in Table VII - the model predictions are in line with the data within 15%. The yields of various particle species produced in pp collisions at 205 GeV/c ($\sqrt{s} \approx 19.7$ GeV) [52] are listed in Table VIII. It is easy to see that the model predictions lie generally well within the 10% of the data except for the strange baryons. Table IX presents the results on particle production in pp interactions at $\sqrt{s} = 27$ GeV [58]. Again, the agreement between the experimental and theoretical results is good. As discussed above, the production of $\Lambda(\bar{\Lambda})$'s is overestimated by a factor of 2-3 due to the neglect of finite size effects in the strings.

The rapidity spectra of pions and x_F -distributions of baryons, as obtained from the UrQMD model for pp interactions at 205 GeV/c (Fig. 30 and 31, respectively) have been discussed already in the previous section. Correlations between the transverse and longitudinal momenta of charged pions, produced in the same reaction, can be studied [52]. The

²Temperatures have been extracted from a statistical model fit to the particle yields in pp , $\bar{p}p$ and e^+e^- .

transverse momenta of both positively and negatively charged pions have evident minima at $x_F = 0$ as shown in Fig. 36 (the "sea-gull" effect). Then the transverse momentum increase nearly linearly with the rising longitudinal momenta. The agreement with the experimental data is fair. The single event correlation between the transverse momenta of the produced pions and the multiplicity of the negatively charged hadrons in the event is presented in Fig. 37. The measured distribution is reproduced nicely for π^+ 's, while for the π^- 's, 20% deviations of the calculated spectrum from the data are evident at high ($n_{h^-} \geq 5$) event multiplicities.

To probe the ability of the UrQMD model to describe hadron-hadron collision even at the today highest available bombarding energies for nuclei, we compare the calculated He+He collision at ISR with data [53] as shown in Fig. 38.

It is not surprising, that the light helium system is transparent. A baryon free area of 3 units in rapidity is produced. The UrQMD model prediction describes the data fairly well. The calculated particle yields can be increased by 15% if one includes multiple jet creation into the model description [54].

The UrQMD model reproduces the cross-sections and spectra of particles in hadronic collisions fairly well. Since hadronic interactions build up the basic input to simulate the hadron-nucleus and nucleus-nucleus interactions in the model, it is interesting to examine the applicability of the UrQMD model to these reactions. The full comparison with the experimental hA and AA data is an ongoing program, which is not completed yet [59].

The ability of the model to reproduce e.g. dilepton yields in pp collisions, which is of interest in high energy physics is shown here as an example. Fig. 39 shows the UrQMD calculations of the dilepton spectrum for $p+\text{Be}$ (which serves as a substitute for pp reactions) at 450 GeV/c. Dilepton sources considered here are Dalitz decays (π^0 , η and ω) and direct vector meson decays (ρ , ω and ϕ). Dalitz decays of heavier meson and baryon resonances are included explicitly via their emission of ρ mesons (assuming vector meson dominance). To avoid double counting, the ρ mesons from η 's, and ω 's are excluded from the ρ contribution. Pion annihilation is included dynamically into the contribution of decaying ρ mesons via the channel $\pi^+\pi^- \rightarrow \rho \rightarrow e^+e^-$. The calculation of dilepton yields without modifications of the ρ mass pole is compatible with the CERES data [55].

VII. SUMMARY

The basic hadronic interaction processes incorporated into the UrQMD approach are given. The implemented cross-sections of various hadron-hadron collisions, as well as their extrapolations into the high energy region are presented. The model treatment of excitation and decay of intermediate objects like resonances and strings is described. The importance of the finite size effects for the process of string fragmentation is discussed. The UrQMD model is a microscopic transport model which allows to study optionally color fluctuations, i.e. color coherence phenomena, as Color Transparency and Color Opacity, as well as the expansion of small wave packets from the point of the production. The model predictions are compared with the available experimental data on particle yields in hadronic interactions for a wide range of c.m. energies. The UrQMD model treats the elementary processes reasonably well. More accurate data on proton-proton, proton-neutron, as well as meson-baryon collisions are needed to improve the extrapolation to nucleus-nucleus interactions at

high energies, where already in the present model - about 10^4 elementary hadron-hadron reactions are possible.

ACKNOWLEDGEMENTS

This work was supported by the Graduiertenkolleg für Theoretische und Experimentelle Schwerionenphysik, Frankfurt–Giessen, the Bundesministerium für Bildung und Forschung, the Gesellschaft für Schwerionenforschung, Darmstadt, Deutsche Forschungsgemeinschaft, the Alexander von Humboldt–Stiftung, the Josef Buchmann-Stiftung, DAAD and in part by DOE grant DE-FG02-96ER40945.

REFERENCES

- [1] Quark Matter'96, Heidelberg, Germany, Nucl. Phys. A **610** (1996); Quark Matter'97, Tsukuba, Japan, Nucl. Phys. A **638** (1998); S. A. Bass, M. Gyulassy, H. Stöcker, W. Greiner, J. Phys. G (1998) in print ; Strange Quark Matter '97, J. Phys. G **23** (1997); Strange Quark Matter '98, J. Phys. G (1998).
- [2] L.D. Landau, Izv. Acad. Nauk USSR **17**, 51 (1953); L.D. Landau and S.Z. Belenkij, Nuovo Cimento, Supplement **3**, 15 (1956).
- [3] T. Regge, Nuovo Cimento **14**, 951 (1959); V.N. Gribov, Sov. Phys. JETP **53**, 654 (1967).
- [4] L.D. Landau, E.M. Lifshitz, Fluid Mechanics (Pergamon, Oxford, 1959) ; H. Stöcker, W. Greiner, Phys. Rep. **137**, 277 (1986); R.B. Clare, D. Strottman, Phys. Rep. **141**, 177 (1986); E. Schnedermann, J. Sollfrank, U. Heinz, Phys. Rev. C **48**, 2462 (1993); J. Brachmann, A. Dumitru, J. Maruhn, H. Stöcker, W. Greiner, D. Rischke, Nucl. Phys. A **619**, 391 (1997).
- [5] S.A. Bass, M. Belkacem, M. Bleicher, M. Brandstetter, L. Bravina, C. Ernst, L. Gerland, M. Hofmann, S. Hofmann, J. Konopka, G. Mao, L. Neise, S. Soff, C. Spieles, H. Weber, L.A. Winkelmann, H. Stöcker, W. Greiner, Ch. Hartnack, J. Aichelin, N. Amelin, Prog. Part. Nucl. Phys. **41**, 225 (1998).
- [6] B. Anderson, G. Gustafson, G. Ingelman, T. Sjöstrand, Phys. Rep. **97**, 31 (1983).
- [7] K. Werner, Phys. Rep. **232**, 87 (1993).
- [8] N.S. Amelin, L.V. Bravina, L.I. Sarycheva, L.N. Smirnova, Sov. J. Nucl. Phys. **51**, 327 (1990).
- [9] H. Sorge, H. Stöcker, W. Greiner, Ann. Phys. (N.Y.) **192**, 266 (1989).
- [10] A. Capella, U. Sukhatme, C.-I. Tan, J. Tran Thanh Van, Phys. Rep. **236**, 227 (1994).
- [11] M. Gyulassy and X.N. Wang, Comp. Phys. Commun. **83**, 307 (1994).
- [12] J. Aichelin and H. Stöcker, Phys. Lett. B **176**, 14 (1986).
- [13] C.M. Ko, Q. Li, R. Wang, Phys. Rev. Lett. **59**, 1048 (1987); W. Botermans and R. Malfliet, Phys. Rep. **198**, 115 (1990); W. Cassing and U. Mosel, Prog. Part. Nucl. Phys. **25**, 235 (1990).
- [14] K. Geiger, Phys. Rep. **258**, 237 (1995).
- [15] Particle Data Group, Phys. Rev. D **54** (1996).
- [16] H. Calen et al, Phys. Lett. B **366**, 39 (1996).
- [17] A. Donnachie and P. Landshoff, Phys. Lett. B **296**, 227 (1992).
- [18] M. Bleicher, M. Belkacem, C. Ernst, H. Weber, L. Gerland, C. Spieles, S. A. Bass, H. Stöcker, W. Greiner, Phys. Lett. B **435**, 9 (1998)
- [19] S.D. Protopopescu, M. Alston-Garnjost, A. Barbaro-Galtieri, S.M. Flatté, J.H. Freidman, T.A. Lasinski, G.R. Lynch, M.S. Rabin, F.T. Solnitz, Phys. Rev. D **7**, 1279 (1973).
- [20] D. Cohen, T. Ferbel, P. Slattery, B. Werner, Phys. Rev. D **7**, 661 (1973).
- [21] N.B. Durusoy, M. Baubillier, R. George, M. Goldberg, A.M. Touchard, N. Armenise, M.T. Fogli-Muciaccia, A. Silvestri, Phys. Lett. B **45**, 517 (1973).
- [22] M.J. Matison, A. Barbaro-Galtieri, M. Alston-Garnjost, S.M. Flatté, J.H. Freidman, G.R. Lynch, M.S. Rabin, F.T. Solnitz, Phys. Rev. D **9**, 1872 (1974).
- [23] D. Linglin et al., Nucl. Phys. B **57**, 64 (1973).
- [24] E.E. Zabrodin, L.V. Bravina, O.L. Kodolova, N.A. Kruglov, A.S. Proskuryakov,

- L.I. Sarycheva, M.Y. Bogolyubsky, M.S. Levitsky, V.V. Maximov, A.A. Minaenko, A.M. Moiseev, S.V. Chekulaev, Phys. Rev. D **52**, 1316 (1995).
- [25] C.B. Dover, T. Gutsche, M. Maruyama, A. Fässler, Prog. Part. Nucl. Phys. **29**, 87 (1992).
- [26] P. Koch and C.B. Dover, Phys. Rev. C **40**, 145 (1989).
- [27] T. Elioff, L. Agnew, O. Chamberlain, H.M. Steiner, G. Wiegand, T. Ypsilantis, Phys. Rev. **128**, 869 (1962).
- [28] F.E. Close, *Introduction to Quarks and Partons*, (Academic Press, London, 1979).
- [29] D.H. Perkins, *Introduction to High Energy Physics*, (Addison-Wesley, 1987), 3rd edition.
- [30] K. Goulios, Phys. Rep. **101**, 169 (1983).
- [31] L. Frankfurt, G. Miller, M. Strikman, Annu. Rev. Nucl. Part. Sci. **44**, 501 (1994).
- [32] G. Baym, Adv. Nucl. Phys. **22**, 101 (1996).
- [33] P. Danielewicz, Ann. Phys. **152** (1984) 239 and 305.
- [34] C. H. Greiner, Ph.D. thesis, Universität Erlangen-Nürnberg, 1992.
- [35] B. Anderson, G. Gustavson, T. Sjoerstrand, Nucl. Phys. B **197**, 45 (1982); B. Anderson, G. Gustavson, B. Soederberg, Z. Phys. C **20**, 317 (1983).
- [36] D. Kharzeev, Phys. Lett. B **378**, 238 (1996).
- [37] S.E. Vance, M. Gyulassy, X.N. Wang, Nucl. Phys. A **638**, 395c (1998).
- [38] A. Capella, B.Z. Kopeliovich, Phys. Lett. B **381**, 325 (1996).
- [39] Review of Particle Properties, Phys. Rev D **50**, 1319 (1994).
- [40] K. D. Born and E. Laermann and R. Sommer, T. F. Walsh, P. M. Zerwas, Phys. Lett. B **329**, 325 (1994)
- [41] R.D. Field and R.P. Feynman, Nucl. Phys. B **136**, (1978).
- [42] W. Heisenberg and H. Euler, Z. Phys. **98**, 714 (1936).
- [43] J. Schwinger, Phys. Rev. **82**, 664 (1951); W. Greiner, B. Müller, J. Rafelski, QED of Strong Fields, Springer Verlag, Heidelberg.
- [44] T.S. Biro, H.B. Nielsen, J. Knoll, Nucl. Phys. B **245**, 449 (1984); H. Sorge, Phys. Rev. C **52**, 3291 (1995); N.S. Amelin, M.A. Braun, C. Pajares, Z. Phys. C **63**, 507 (1994).
- [45] A. Chodos, R.L. Jaffe, K. Johnson, C.B. Thorn, V.F. Weisskopf, Phys. Rev. D **9**, 3471 (1974).
- [46] T. Schönfeld, A. Schäfer, B. Müller, K. Sailer, J. Reinhardt, W. Greiner, Phys. Lett. B **274**, 5 (1990).
- [47] R. Wang and C. Wong, Phys. Rev. D **38**, 348 (1988).
- [48] S. Ben-Hao and T. An, Phys. Rev. C **55**, 2010 (1997).
- [49] G. Mao, Z. Li, Z. Yizhong, H. Yinlu, Y. Ziqiang, M. Sano, Z. Phys. A **347**, 173 (1994); G. Mao, L. Neise, H. Stöcker, W. Greiner, Z. Li, Phys. Rev. C **57**, 1938 (1998).
- [50] F. Becattini, J. Phys. G **23**, 1933 (1997).
- [51] V. Bobel et al., Nucl. Phys. B **69**, 454 (1974); Nucl. Phys. B **129**, 221.
- [52] T. Kafka, R. Engelmann, R. Godbole, J. Hanlon, M. Pratap, H. Wahl, R. Singer, Y. Cho, T. Fields, L.G. Hyman, L. Voyvodic, R. Walker, J. Whitmore, Phys. Rev. D **16**, 1261 (1977); G. Charlton et al., Phys. Rev. Lett. **30**, 574 (1973).
- [53] L. Otterlund, Nucl. Phys. A **418**, 98c (1983).
- [54] T. Schönfeld et al, Mod. Phys. Lett. A **8**, 2631 (1993).
- [55] G. Agakichev et al. (CERES collaboration), Phys. Rev. Lett. **75**, 1272 (1995).
- [56] V. Flaminio et al., CERN-HERA-84-01, 1984.

- [57] M. Antinucci et al., *Lett. Nuov. Cim.* **6**, 121 (1973)
- [58] M. Aguilar-Benetz et al, *Z. Phys. c* **50**, 405 (1991); H. Kichimi et al, *Phys. Rev. D* **20**, 37 (1979); F. Becattini, U. Heinz, *Z. Phys. C* **76**, 269 (1997).
- [59] M. Bleicher et al, submitted to *Phys. Lett. B*; S. Soff et al, manuscript in preparation; S.A. Bass et al, manuscript in preparation.

FIGURES

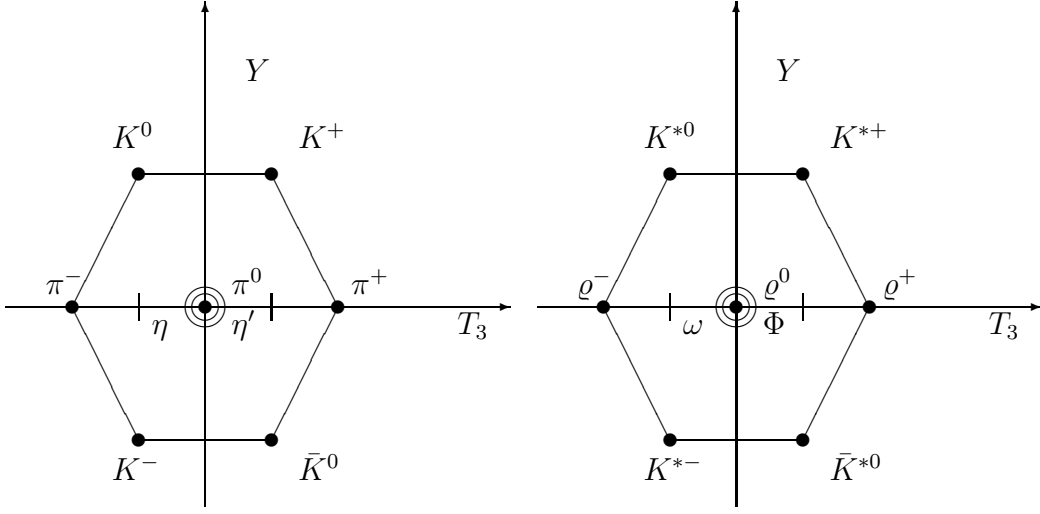


FIG. 1. Implemented mesons: pseudo-scalar mesons (left plot) and vector mesons (right plot).

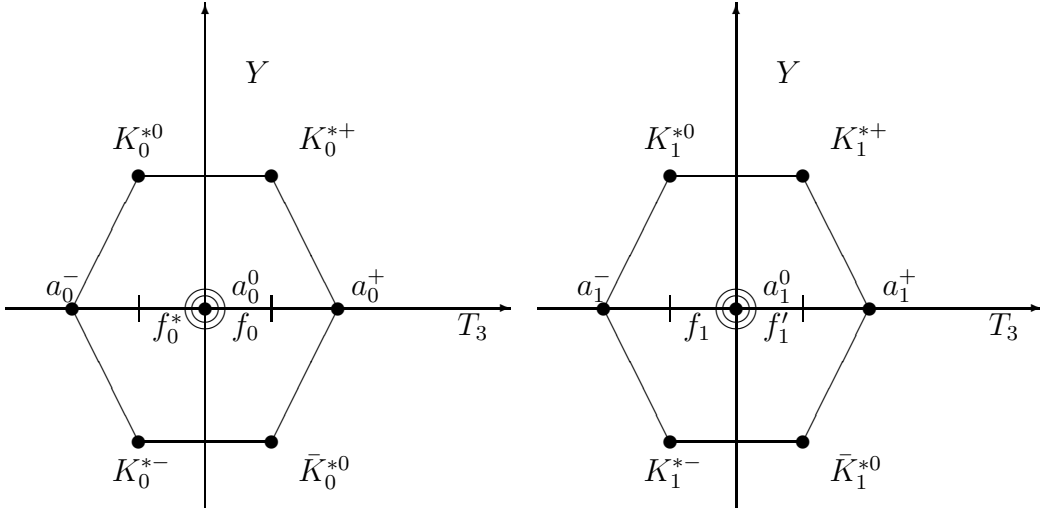


FIG. 2. Implemented mesons: scalar mesons (left plot) and pseudo-vector mesons (right plot). f_1 and f_1' are the states $f_1(1285)$ and $f_1(1420)$, respectively.

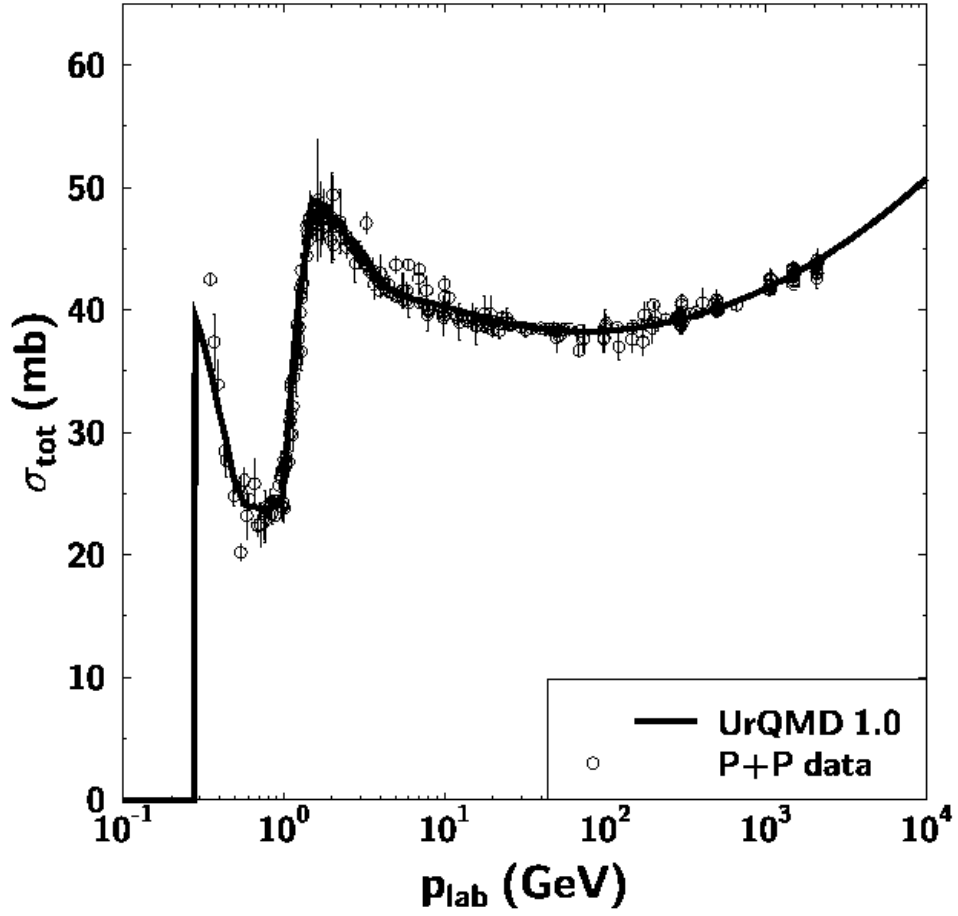


FIG. 3. The total cross-section of pp collisions vs. the laboratory momentum p_{lab} of the incident particle. Data are taken from [15].

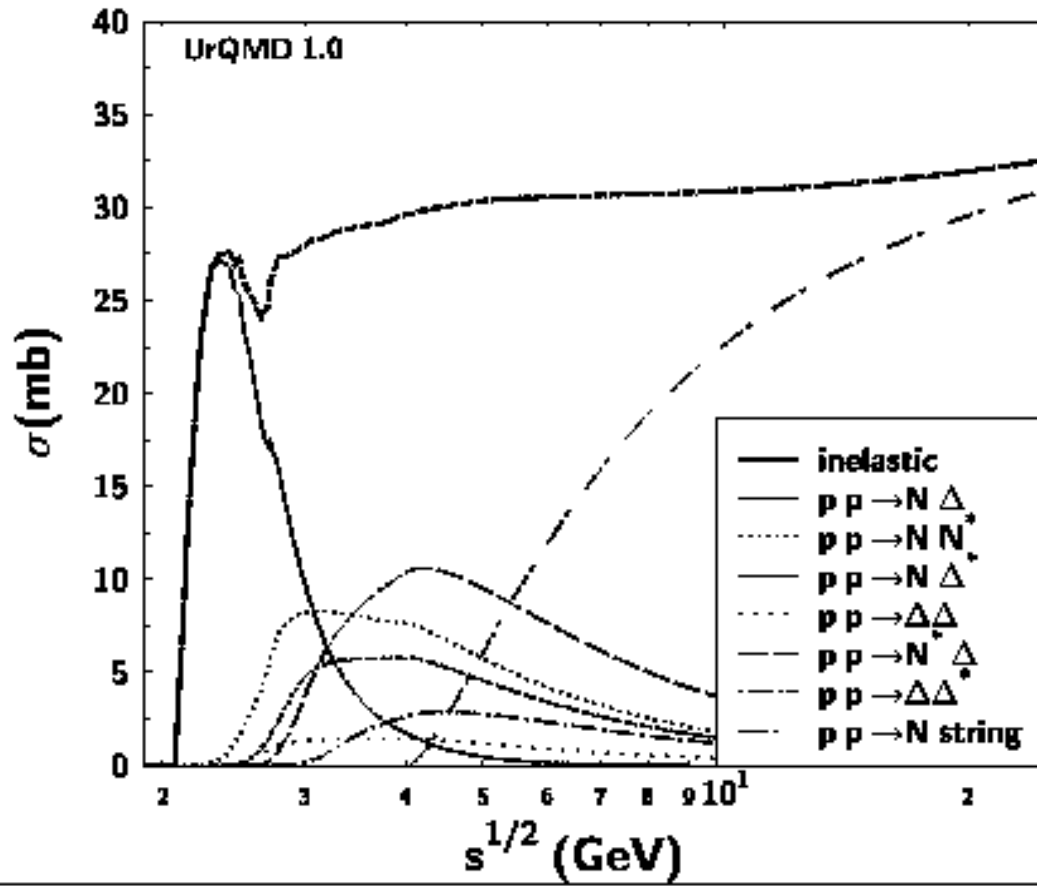


FIG. 4. The inelastic cross-section of pp collisions vs. the laboratory momentum p_{lab} and the cross-sections of the various inelastic channels.

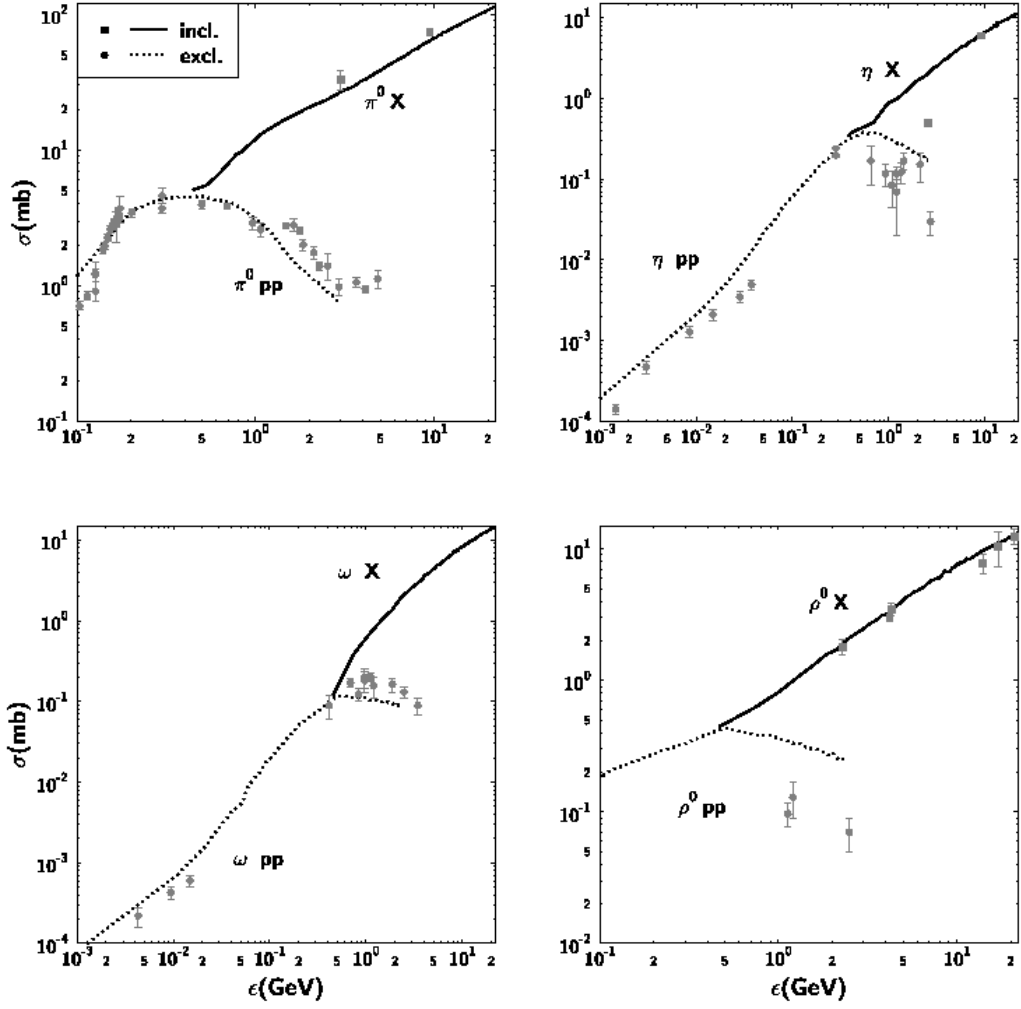


FIG. 5. Cross section for the production of neutral mesons in pp . The inclusive and exclusive meson production is compared to data by [16] [56]

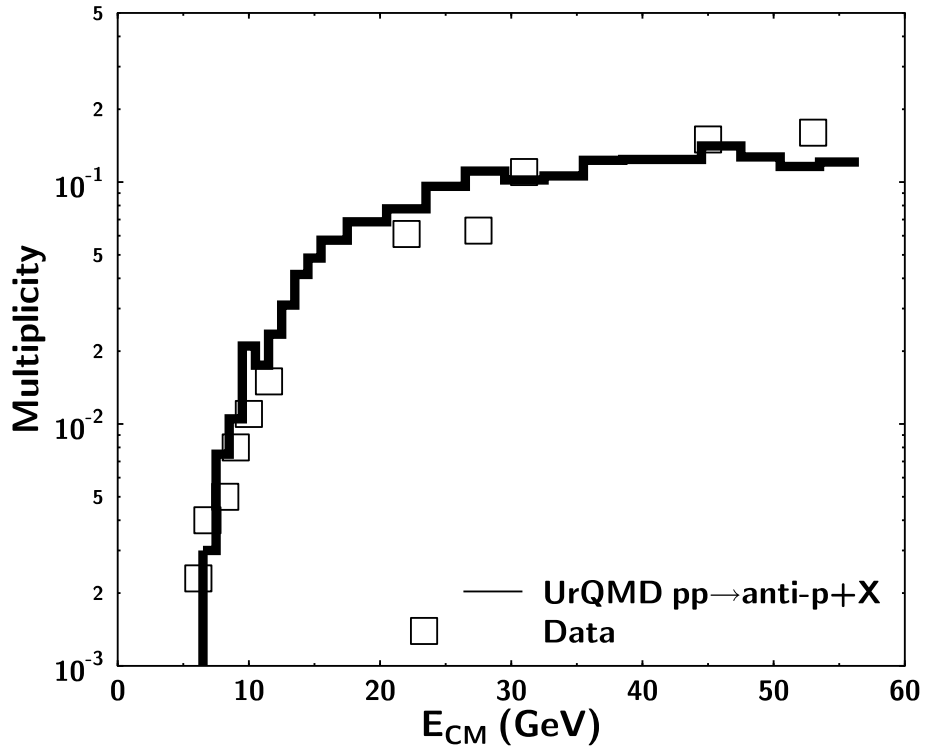


FIG. 6. Cross section for the production of anti-protons in pp as a function of c.m. energy. The UrQMD calculation is compared to data by [57].

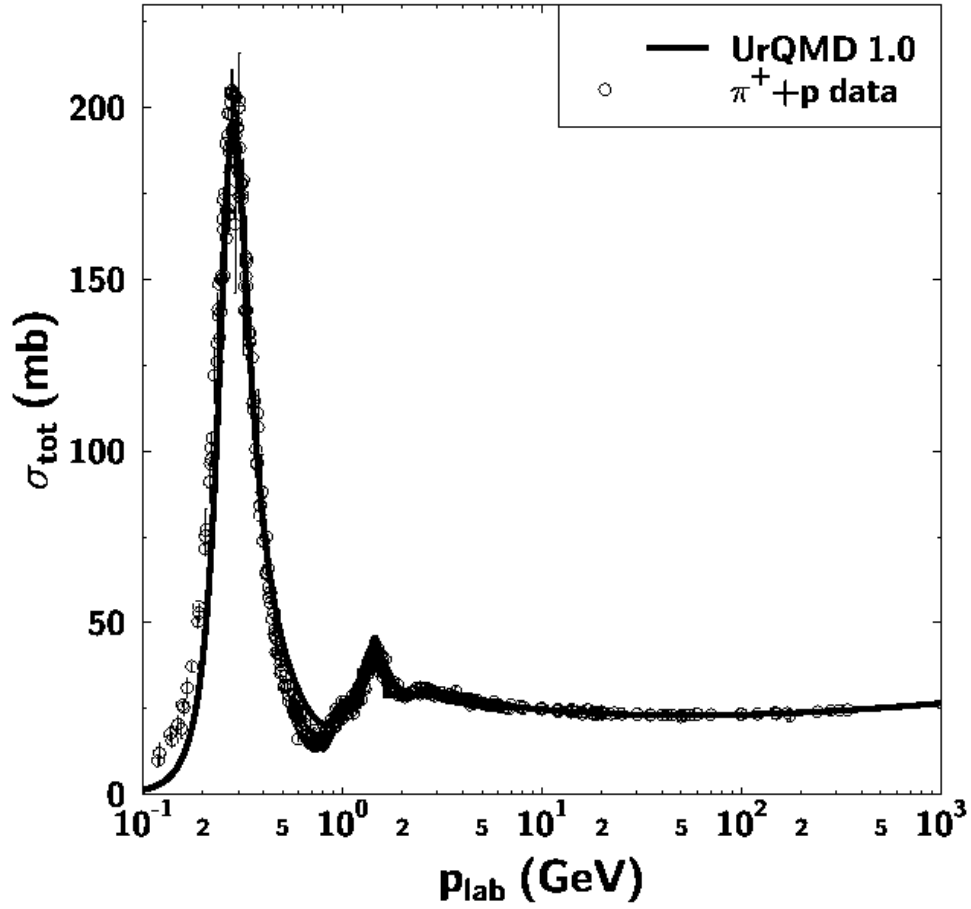


FIG. 7. The total cross-section of π^+p interaction vs. laboratory momentum p_{lab} . Data are taken from [15]. Note that the low energy s-wave π^+p scattering is not included into the UrQMD fit.

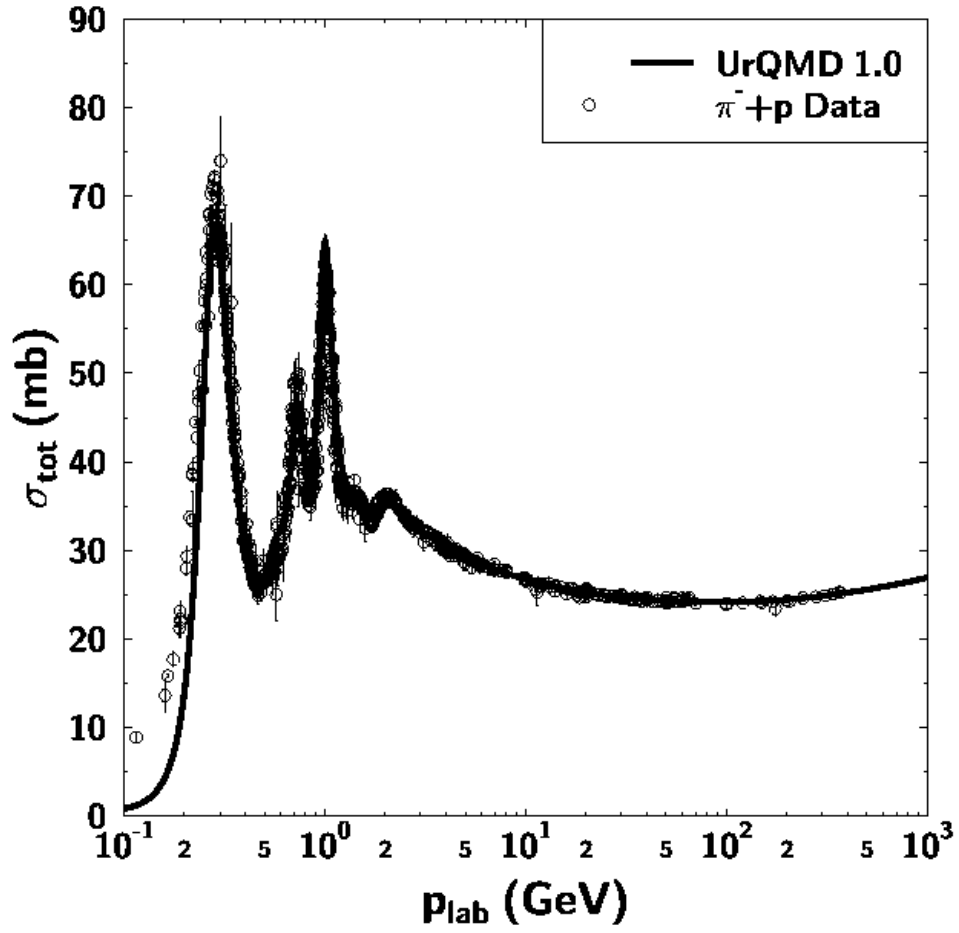


FIG. 8. The same as Fig. 7 but for $\pi^- p$ interaction. Data are taken from [15]. Note that the low energy s -wave $\pi^- p$ scattering is not included into the UrQMD fit.

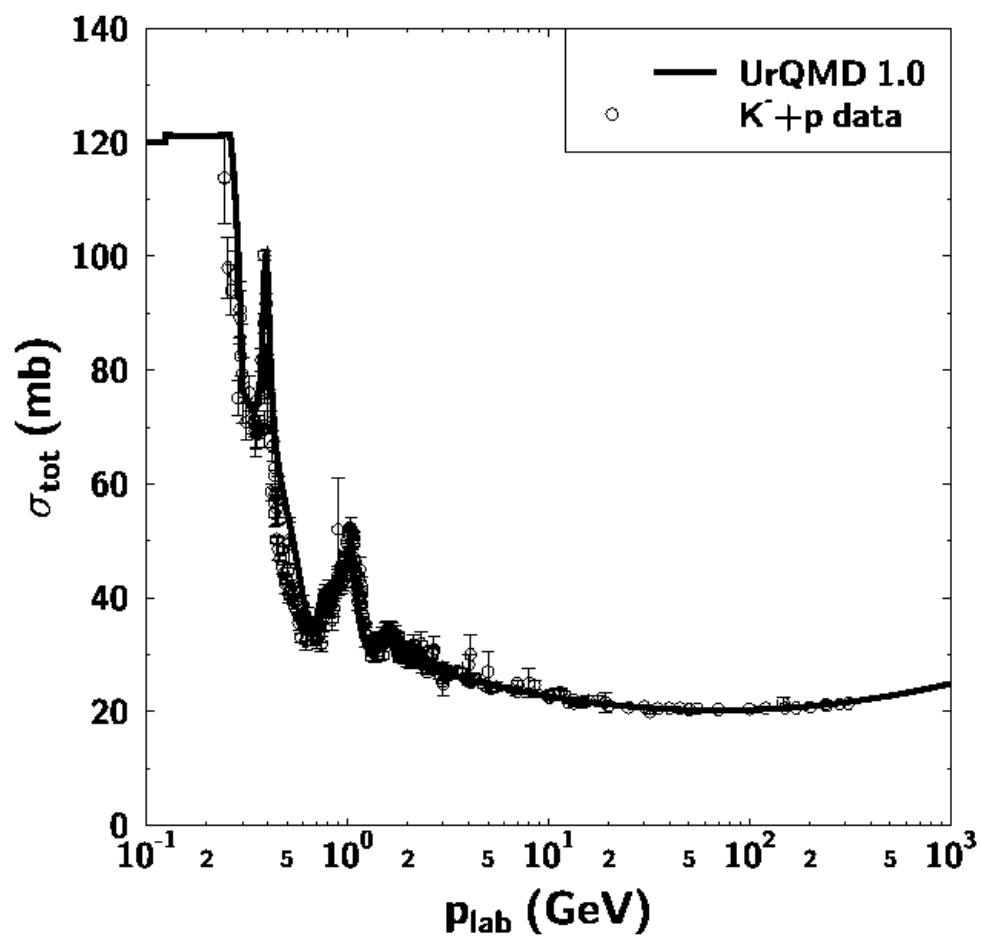


FIG. 9. The same as Fig. 7 but for K^-p reaction. Data are taken from [15].

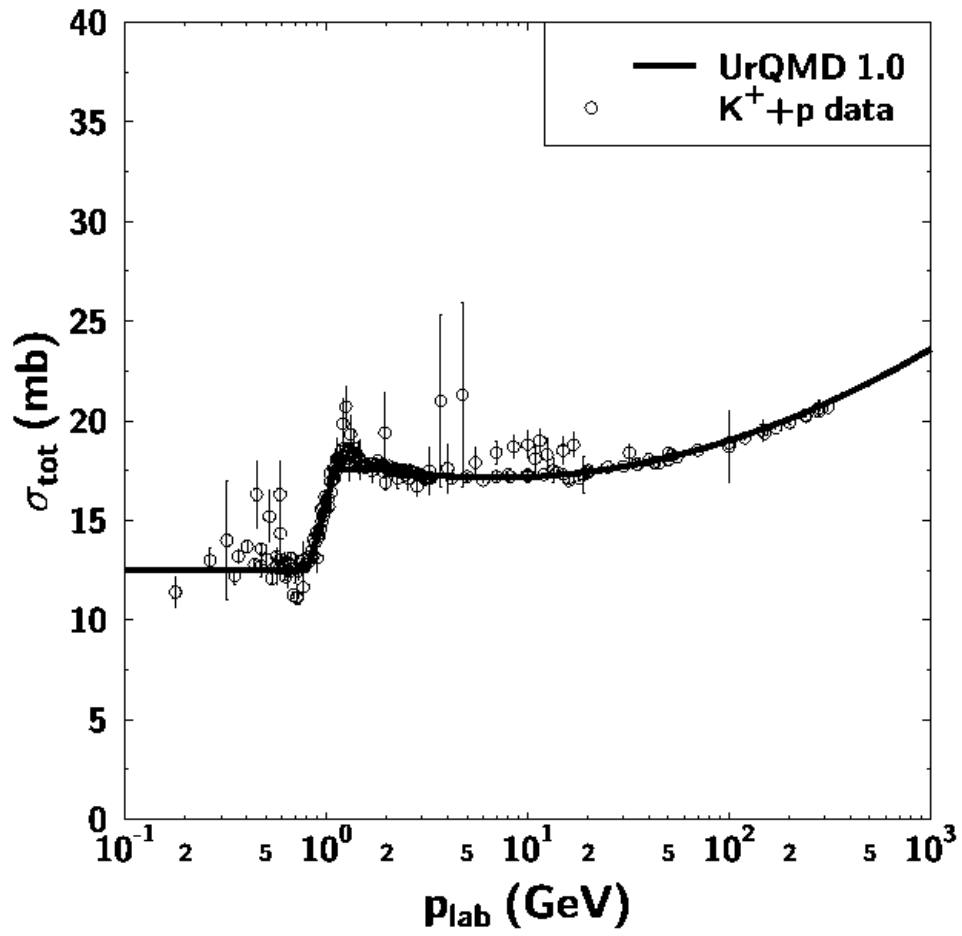


FIG. 10. The same as Fig. 7 but for K^+p reaction. Data are taken from [15].

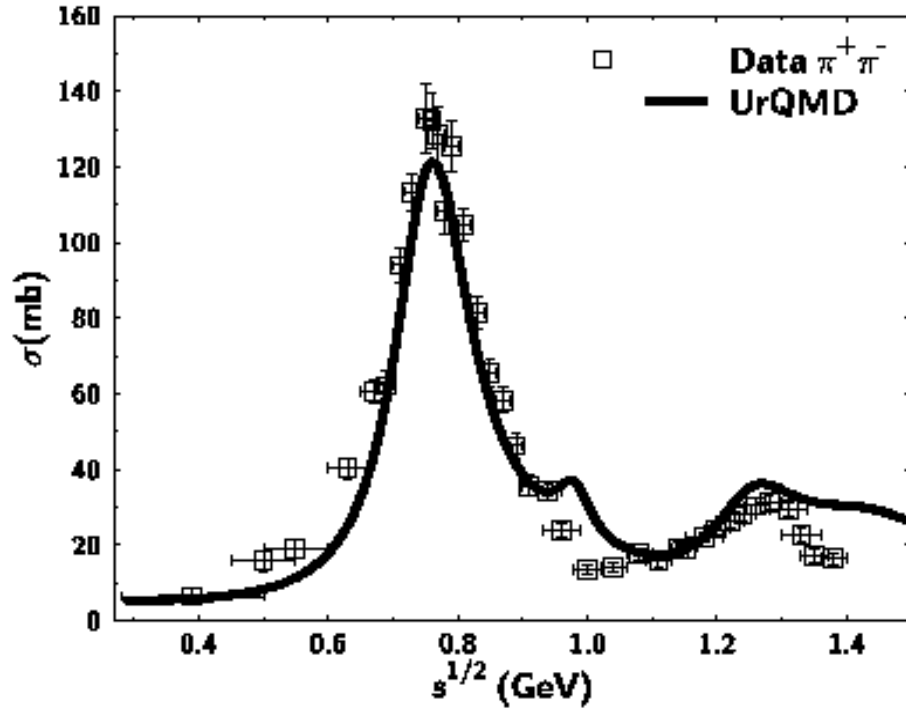


FIG. 11. The total cross-section of $\pi^+\pi^-$ scattering as a function of c.m. energy \sqrt{s} . Data (open squares) are taken from [19].

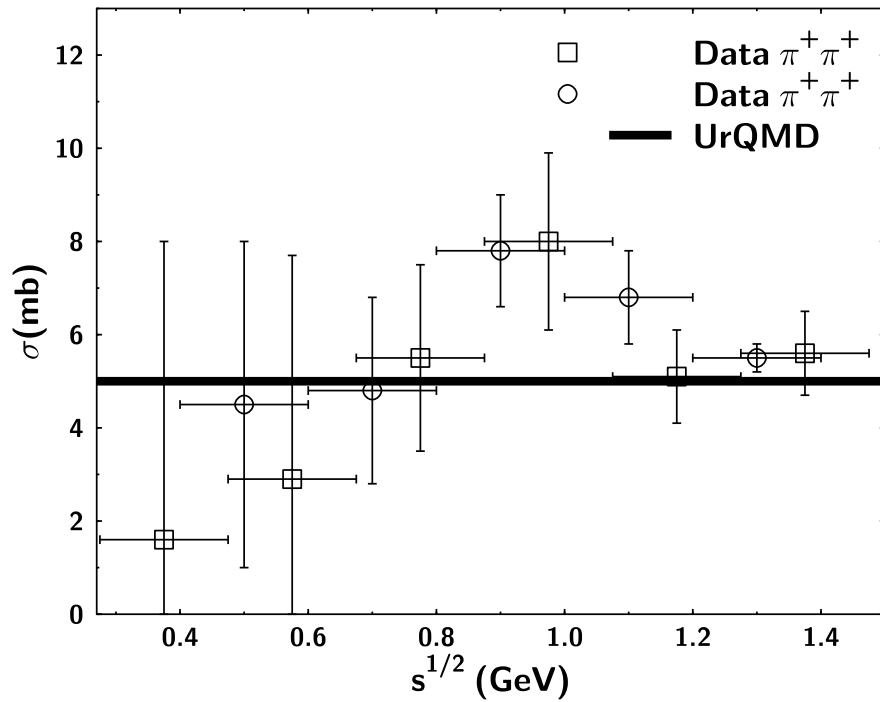


FIG. 12. The same as Fig. 11 but for $\pi^+\pi^+$ scattering. Data are taken from [20] (open squares) and from [21] (open circles).

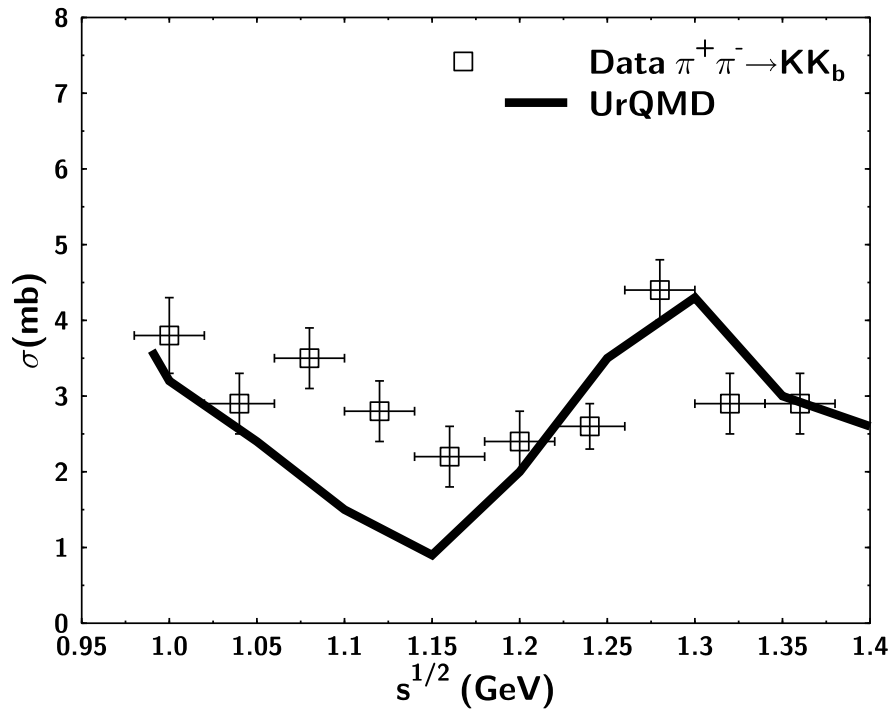


FIG. 13. Cross-section of the reaction $\pi^+\pi^- \rightarrow K\bar{K}$ as a function of \sqrt{s} . Data (open squares) are taken from [19].

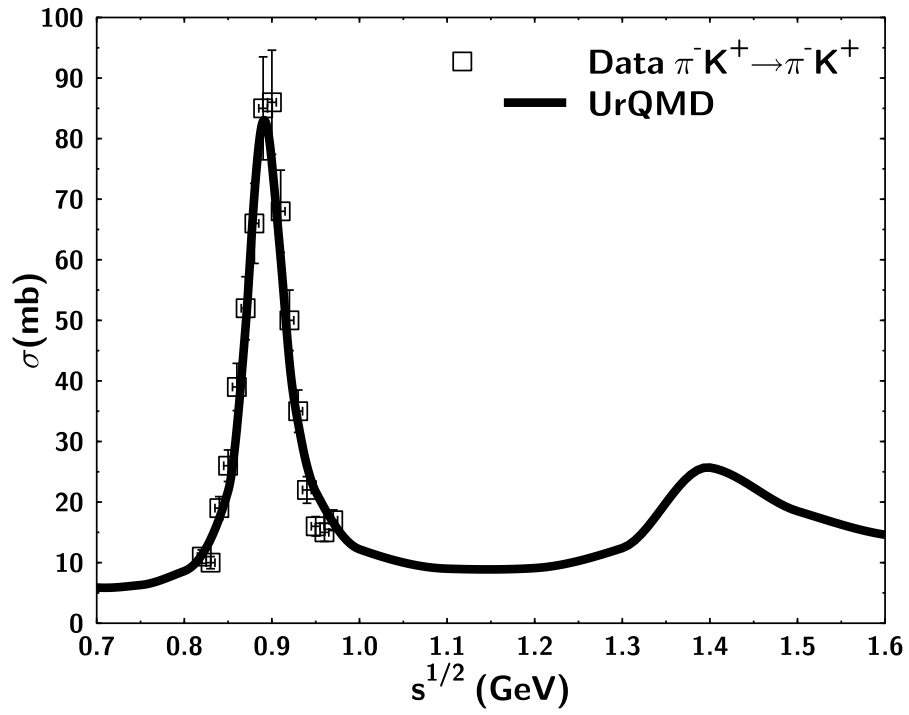


FIG. 14. Cross-section of $\pi^- K^+$ scattering vs. \sqrt{s} . Data (open squares) are taken from [22].

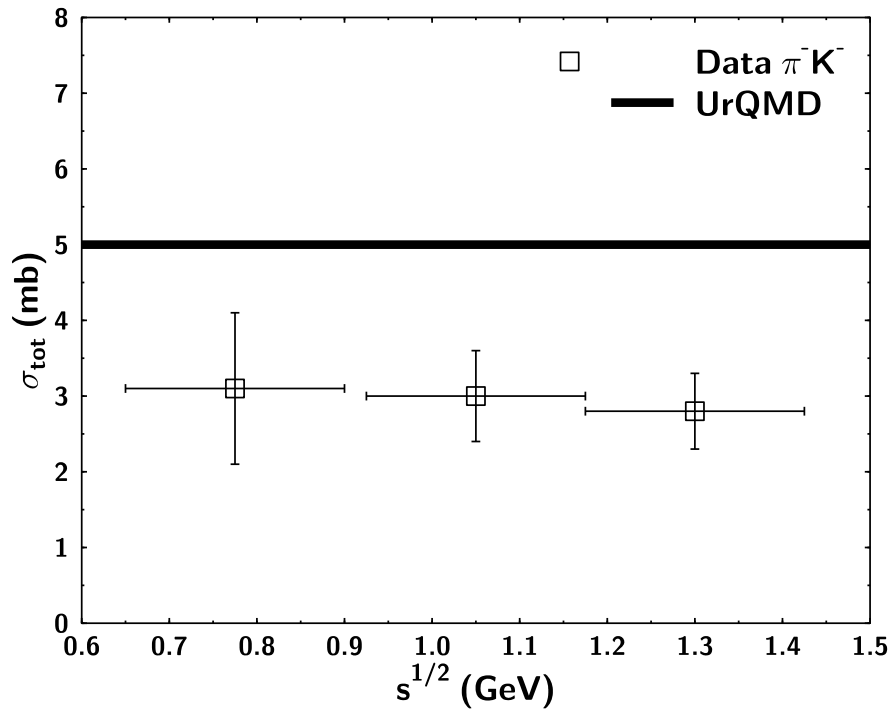


FIG. 15. The same as Fig. 14 but for $\pi^- K^-$ reaction. Data (open squares) are taken from [23].

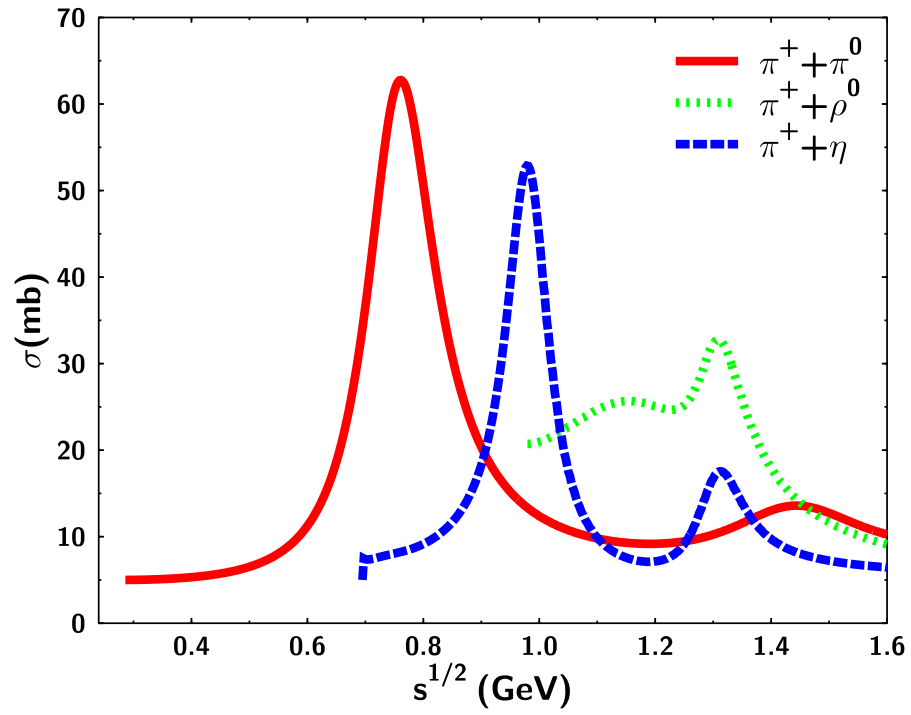


FIG. 16. Cross-sections of $\pi^+\pi^0$ (solid curve), $\pi^+\rho^0$ (dotted curve) and $\pi^+\eta$ (dashed curve) as functions of \sqrt{s} .

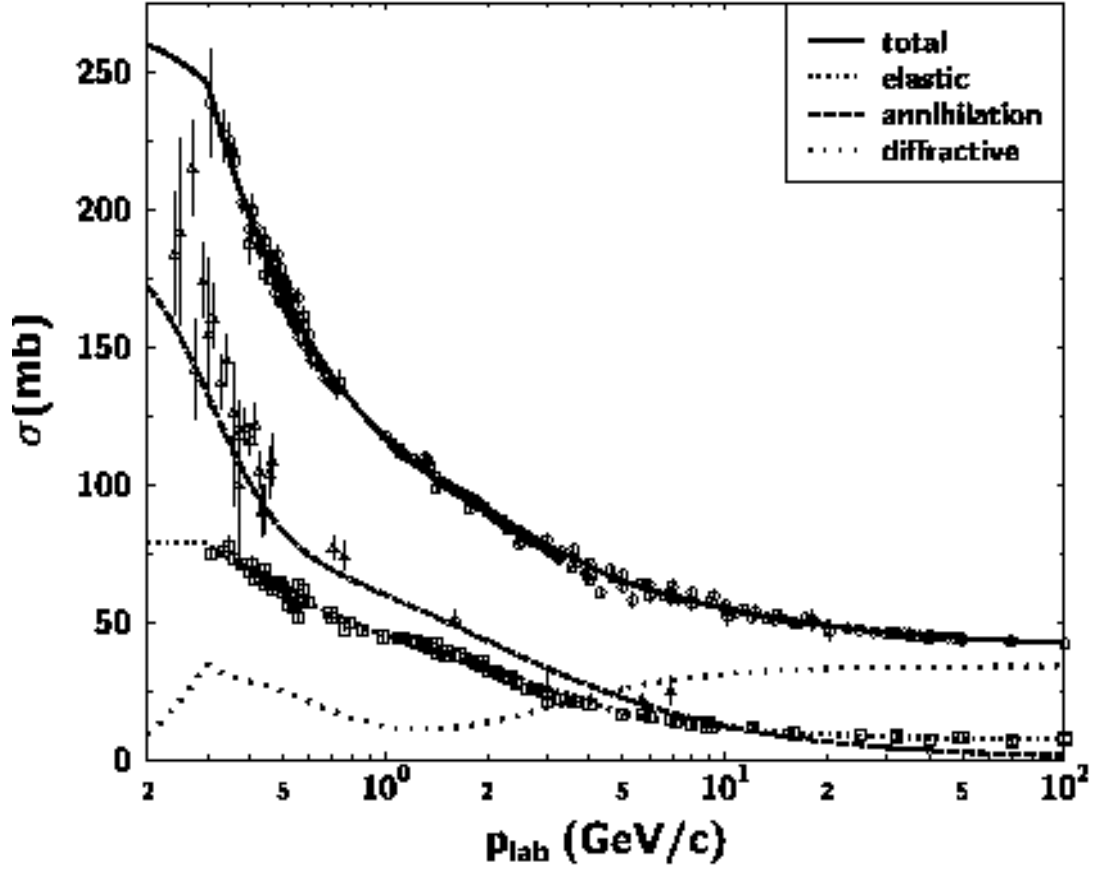


FIG. 17. The $\bar{p}p$ cross-section as compared to the experimental data on total (open circles), elastic (open squares), and annihilation (open triangles) cross-sections. Data are taken from [15]. The diffractive cross-section is assumed to be a difference between the total cross-section and the sum of the elastic and annihilation cross-section.

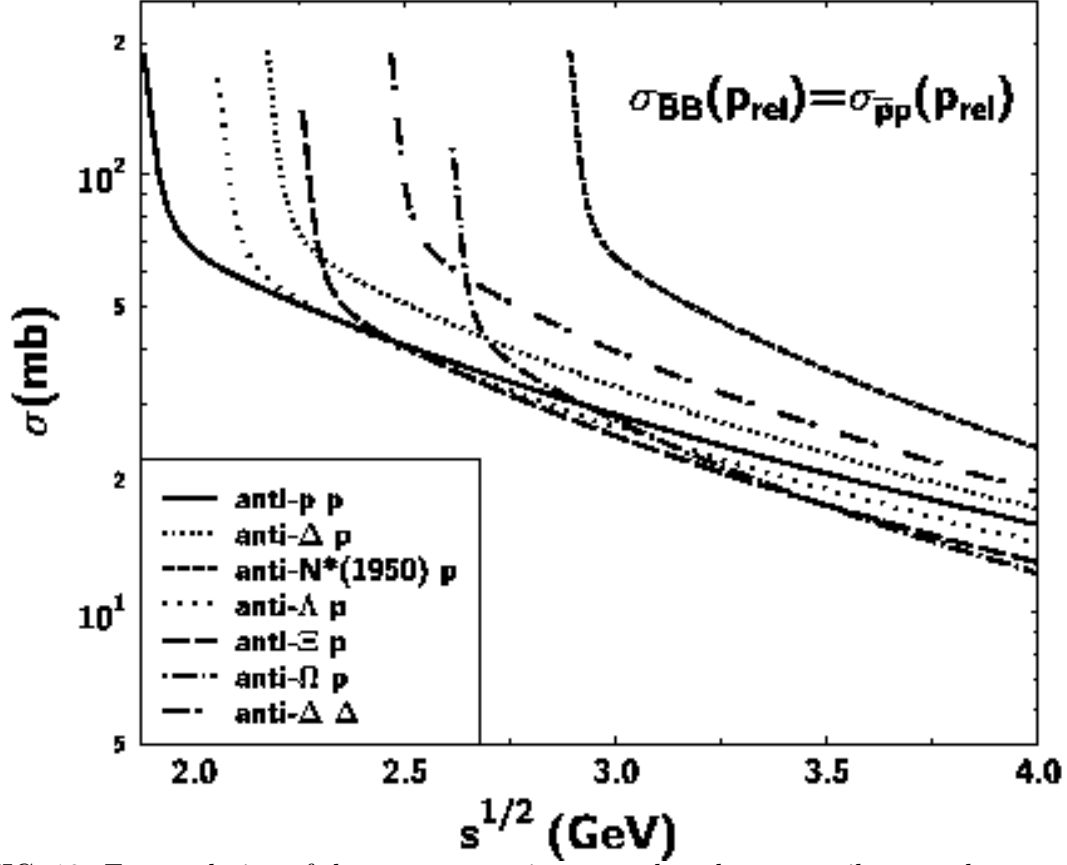


FIG. 18. Extrapolation of the $\bar{p}p$ cross-section towards unknown antibaryon–baryon reactions. Here the cross-section of the antibaryon–baryon interaction is equal to the $\bar{p}p$ cross-section at the same relative momentum. In the UrQMD model we take the antibaryon–baryon cross section equal to the $\bar{p}p$ cross-section at the same center-of-mass energy.

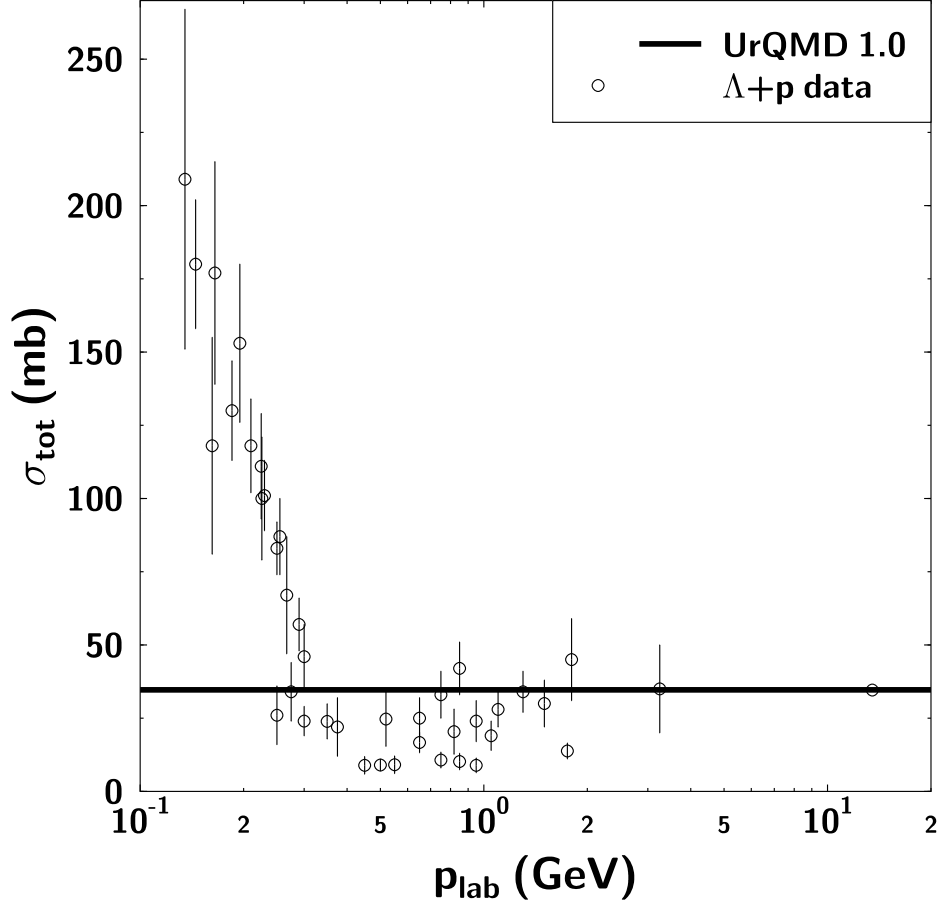


FIG. 19. Total Λ -p cross-section vs. laboratory momentum of the Λ . The UrQMD results are given by the Additive Quark Model. Data are taken from [15]. There seems to be indication for a resonance at $\sqrt{s} = 2.1$ GeV. This could be a 6q molecule or a di-baryon with $s = 1$.

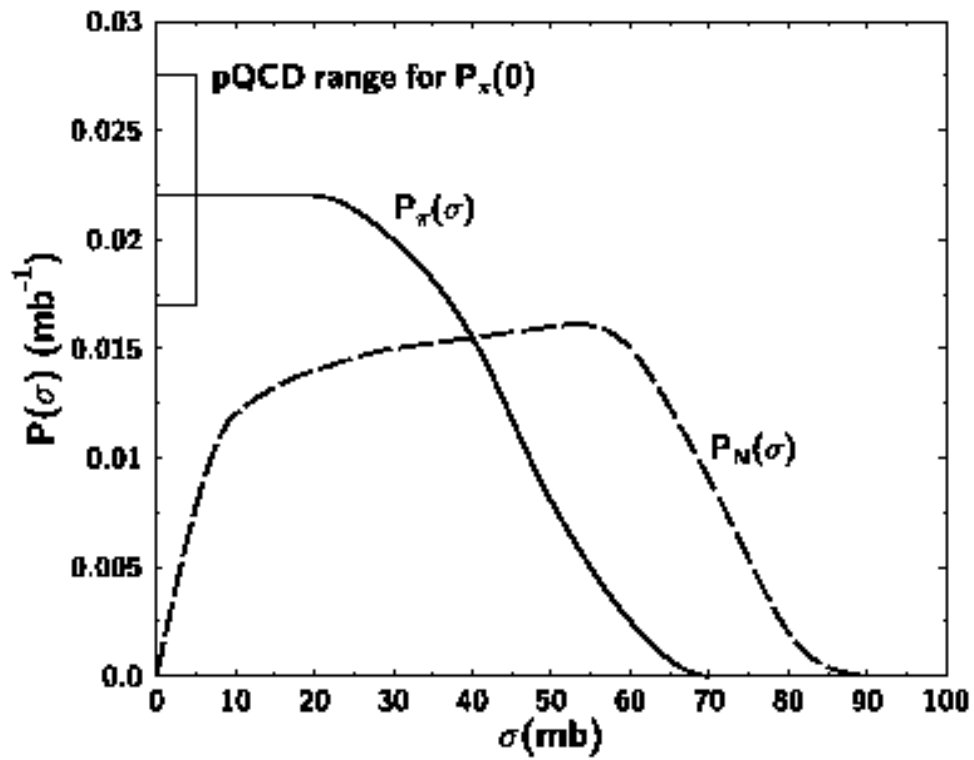


FIG. 20. Probability distribution of nucleon (dashed curve) and pion (solid curve) cross-sections as predicted by [31].

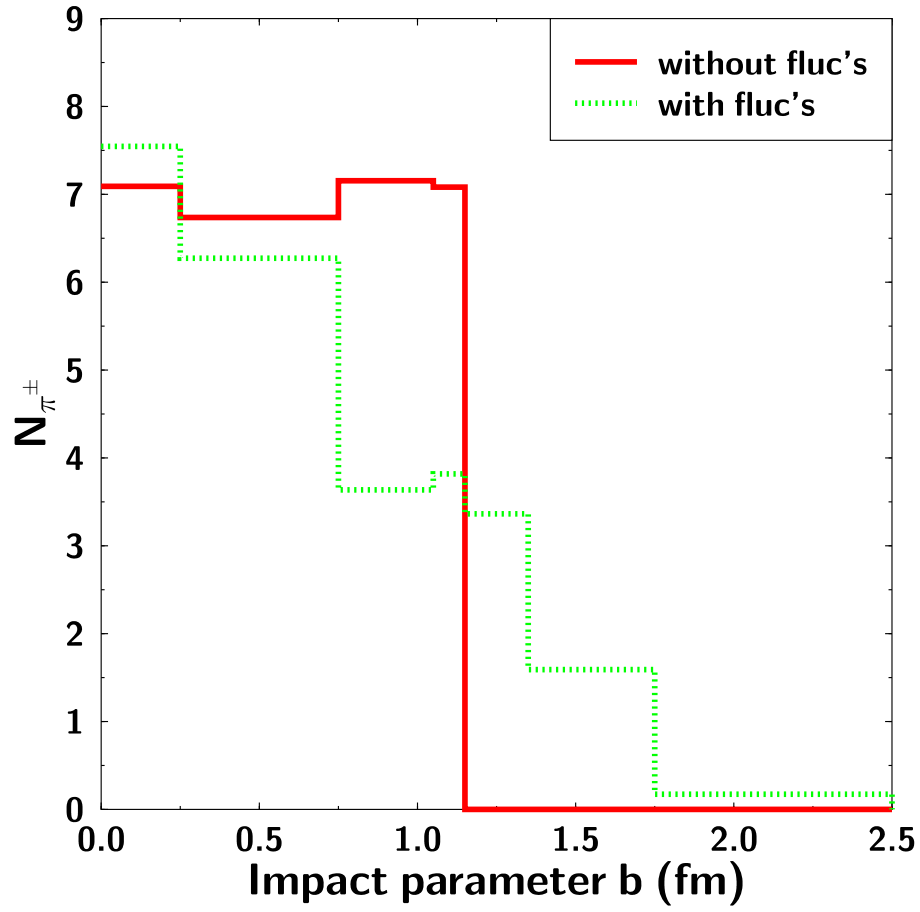


FIG. 21. Charged pion multiplicity in pp collisions at $\sqrt{s} = 27$ GeV with (dotted-) and without (solid-line histogram) color fluctuations for different impact parameters.

p+p exclusive Δ -production

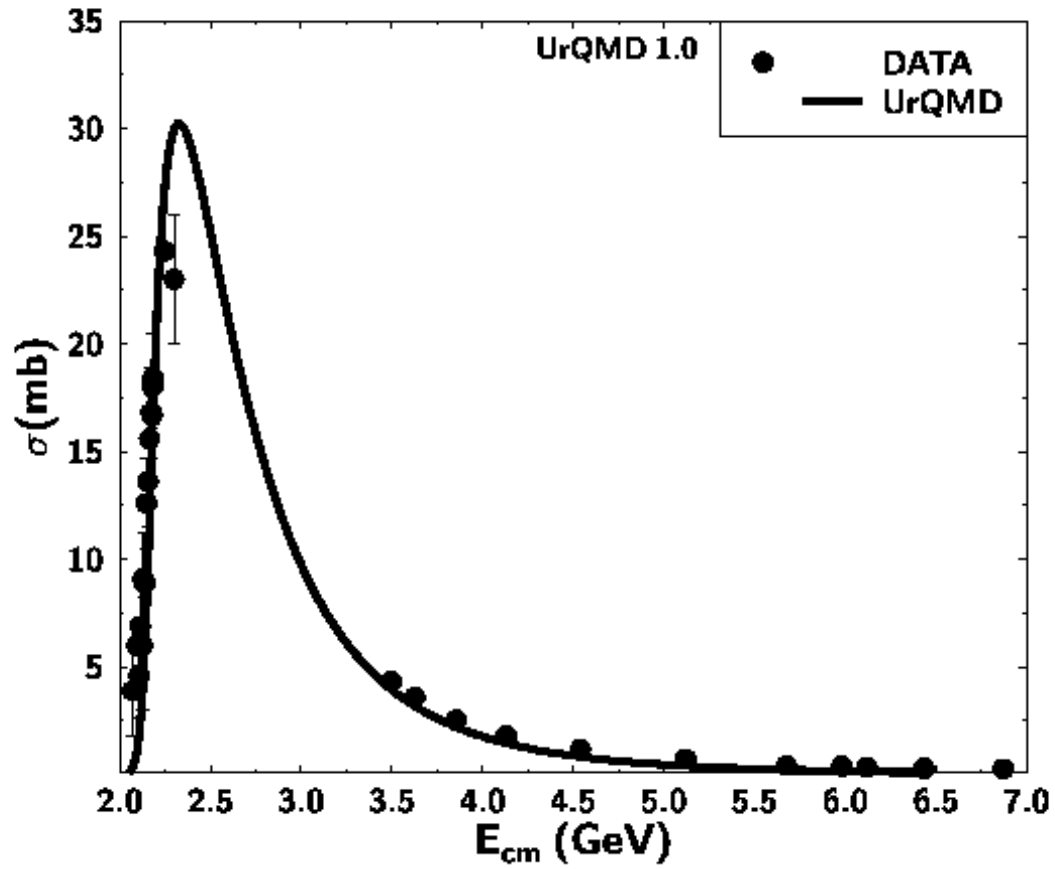


FIG. 22. UrQMD fit for the exclusive Δ_{1232} production in proton-proton reactions compared to data [56].

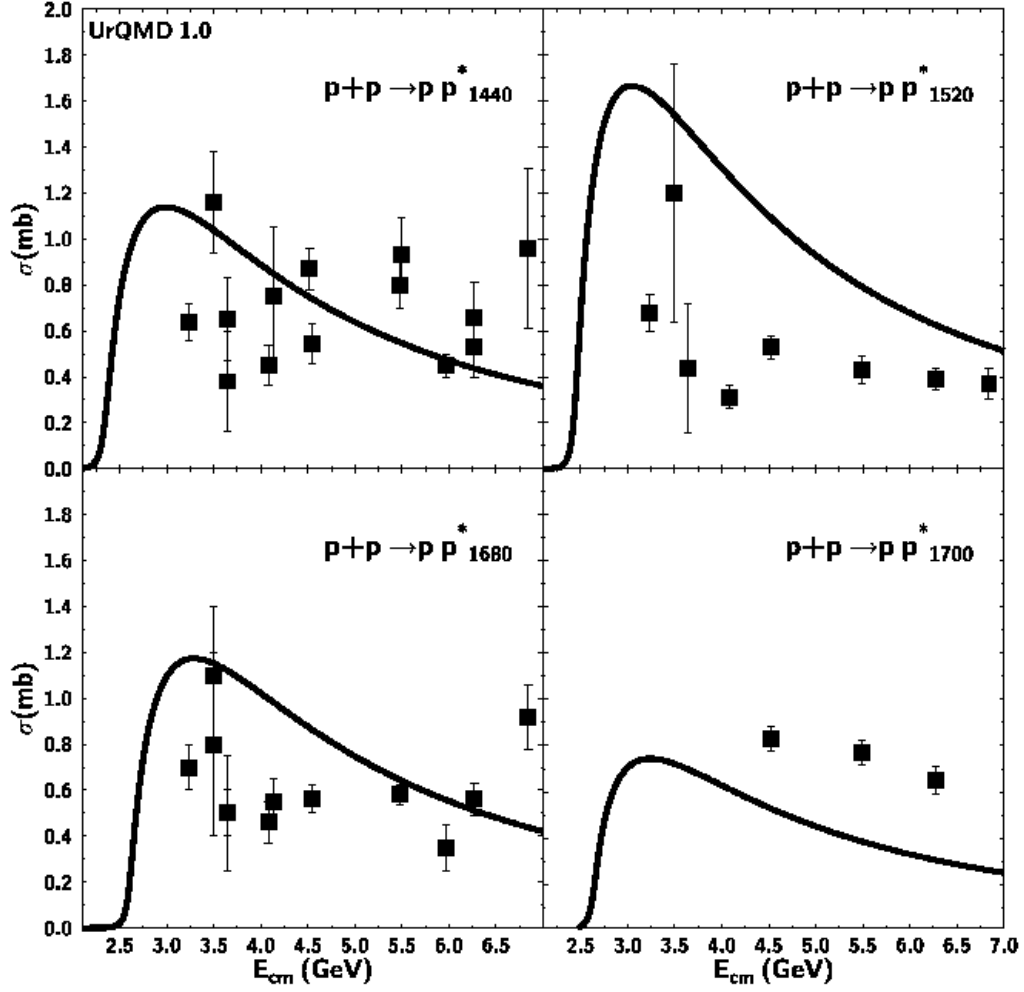


FIG. 23. UrQMD parameterization for exclusive pp^* cross sections. Only one parameter was used to describe all available cross section data [56].

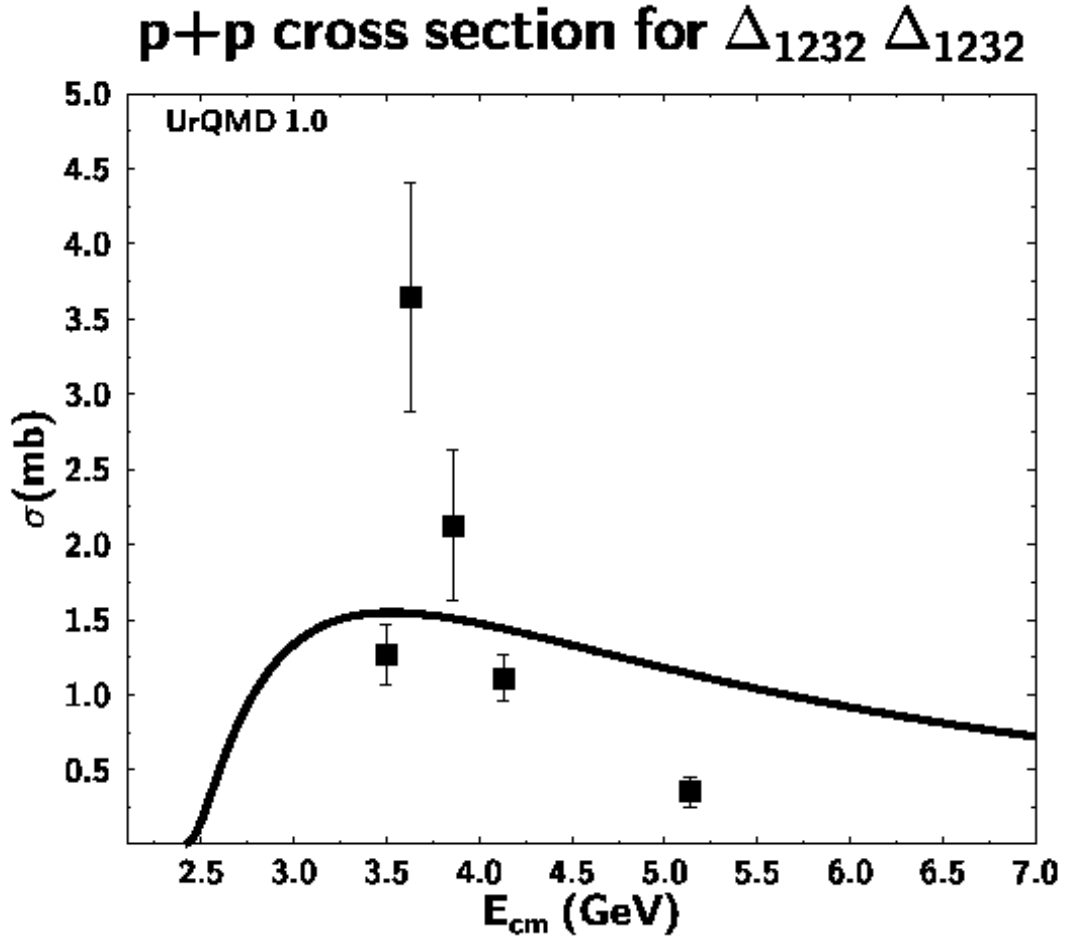


FIG. 24. UrQMD fit for the exclusive $\Delta_{1232}\Delta_{1232}$ production in proton-proton reactions compared to data [56].

p+p cross section for $\Delta_{1920}^* N$

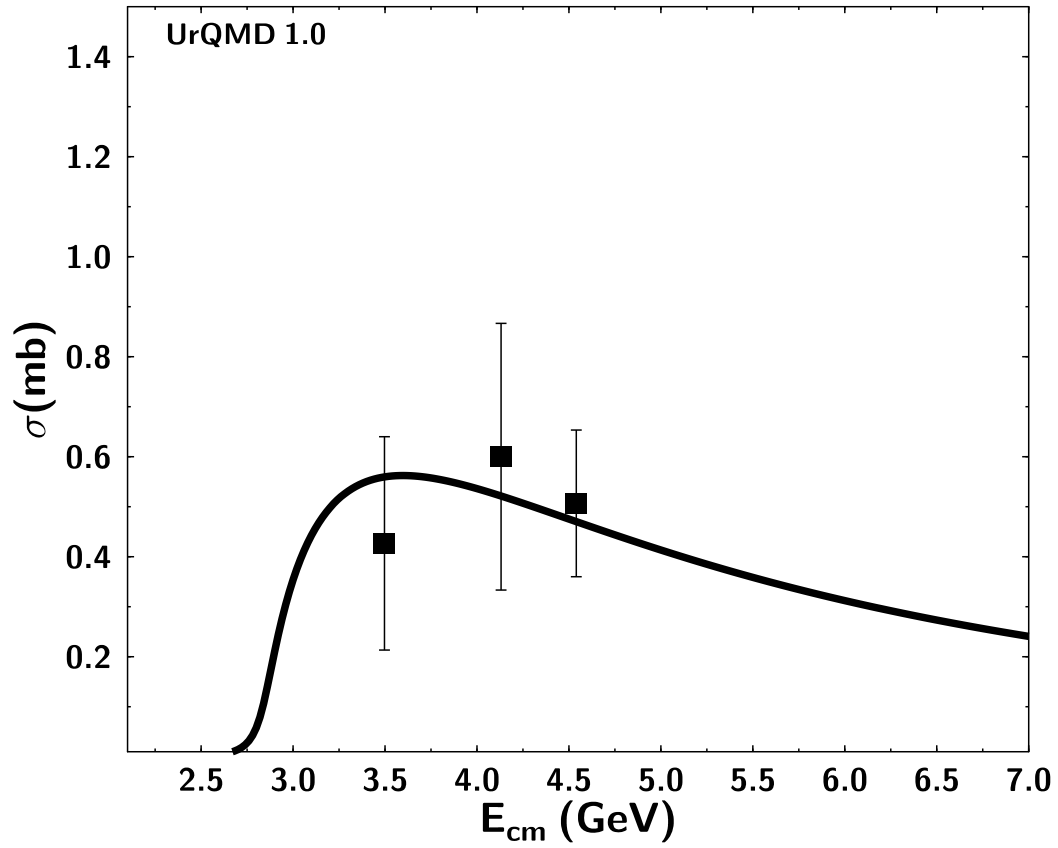


FIG. 25. UrQMD fit for the exclusive $\Delta_{1920}N$ production in proton-proton reactions compared to data [56].

$p+p$ cross section for $\Delta_{1232} N^*_{1680}$

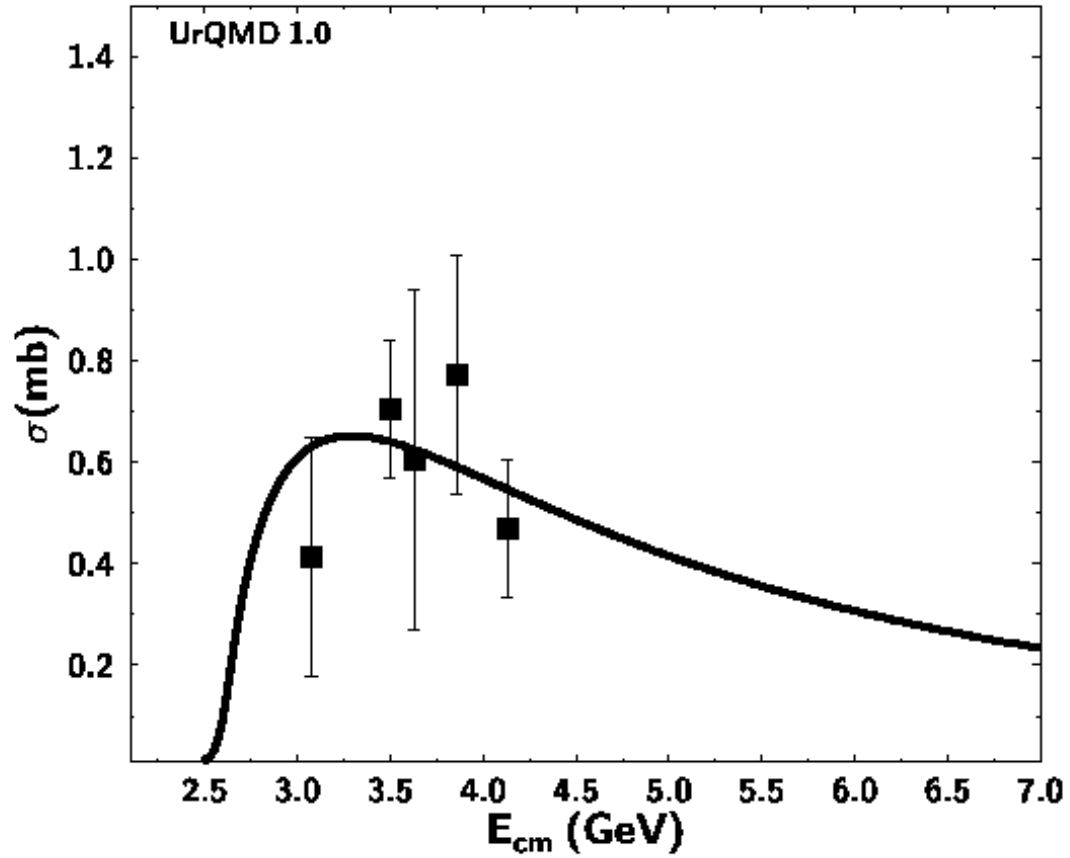


FIG. 26. UrQMD fit for the exclusive $\Delta_{1232}N^*_{1680}$ production in proton-proton reactions compared to data [56]. The matrix element for all $\Delta_{1232}N^*_X$ reactions is extracted from this fit.

p+p cross section for $\Delta_{1232} N_{1520}^*$

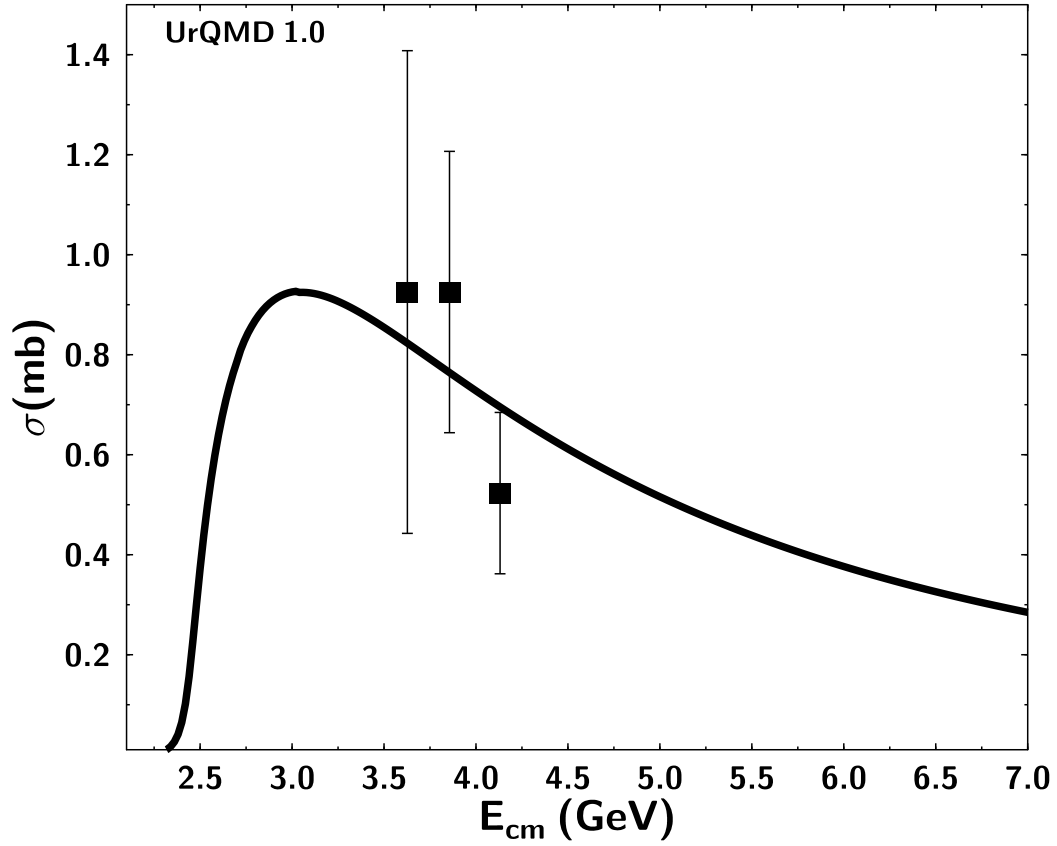


FIG. 27. Comparison between the UrQMD parametrization for the exclusive $\Delta_{1232}N_{1520}^*$ production in proton-proton reactions compared to data [56]. The matrix element has been extracted from a fit to the exclusive $\Delta_{1232}N_{1680}^*$ production.



FIG. 28. Scheme of a decaying string. $s\bar{s}$ and $u\bar{u}$ pairs are created in the color field resulting in a hyperon, a kaon and a pion.

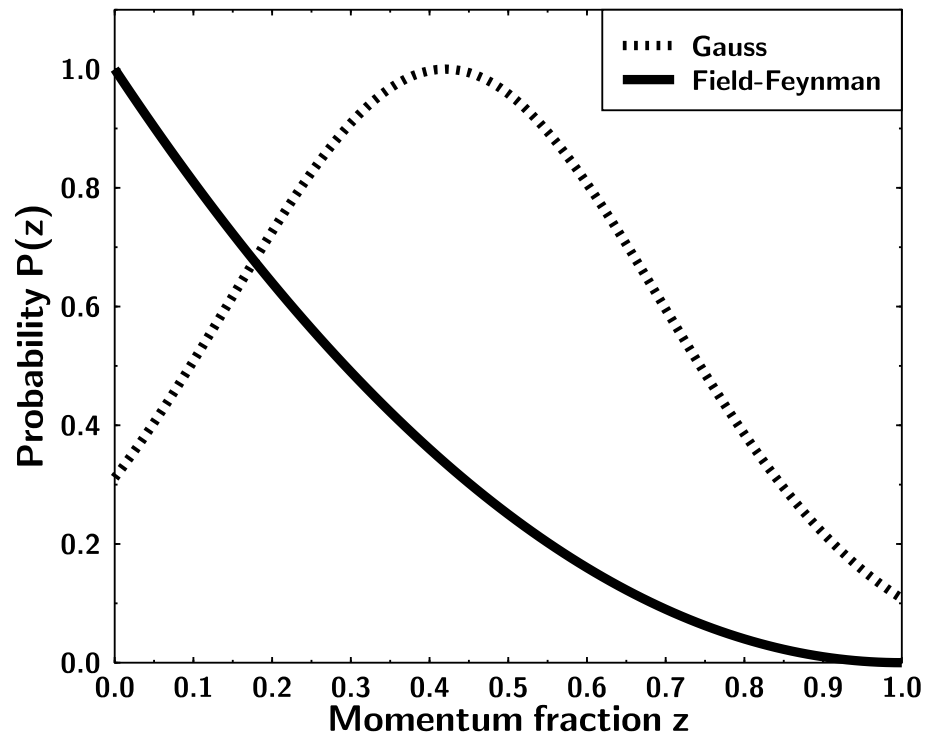


FIG. 29. The Field-Feynman fragmentation function (solid line) is used for newly produced particles. A Gaussian fragmentation function (dashed line) is used for leading baryons.

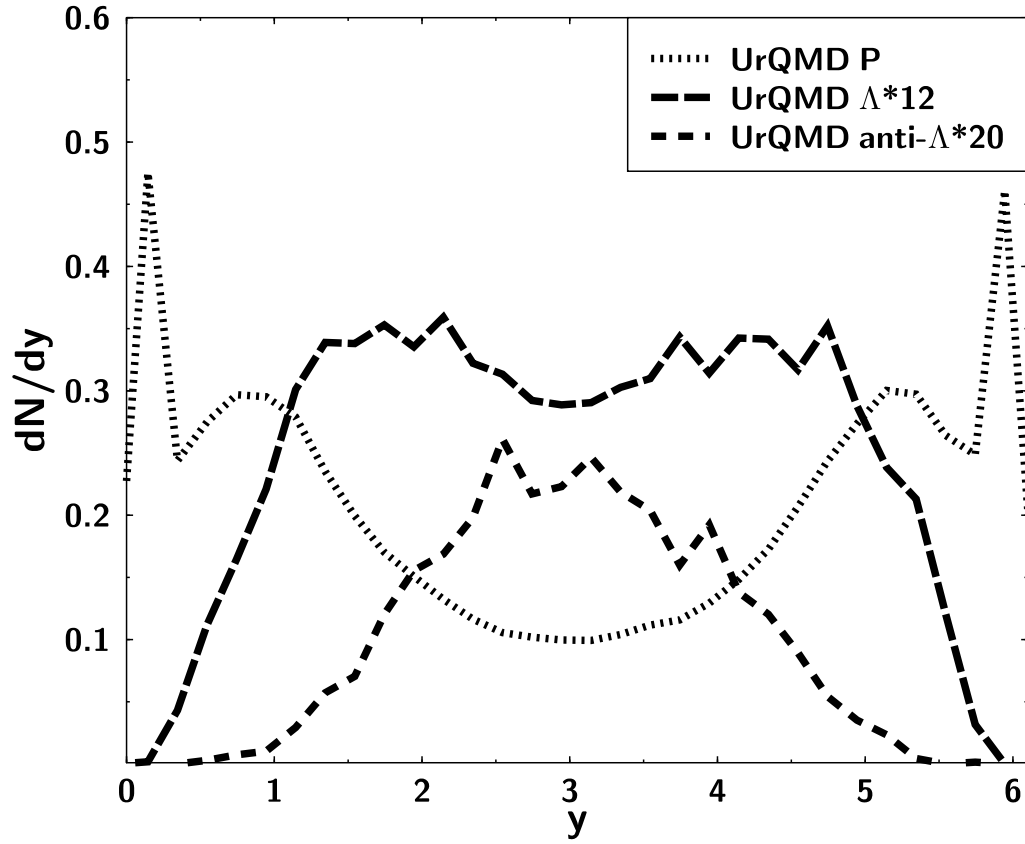


FIG. 30. Rapidity spectrum of protons (dotted curve), Λ 's (dashed) and $\bar{\Lambda}$'s (dash-dotted) for pp collisions at 205 GeV/c. Data are taken from [52].

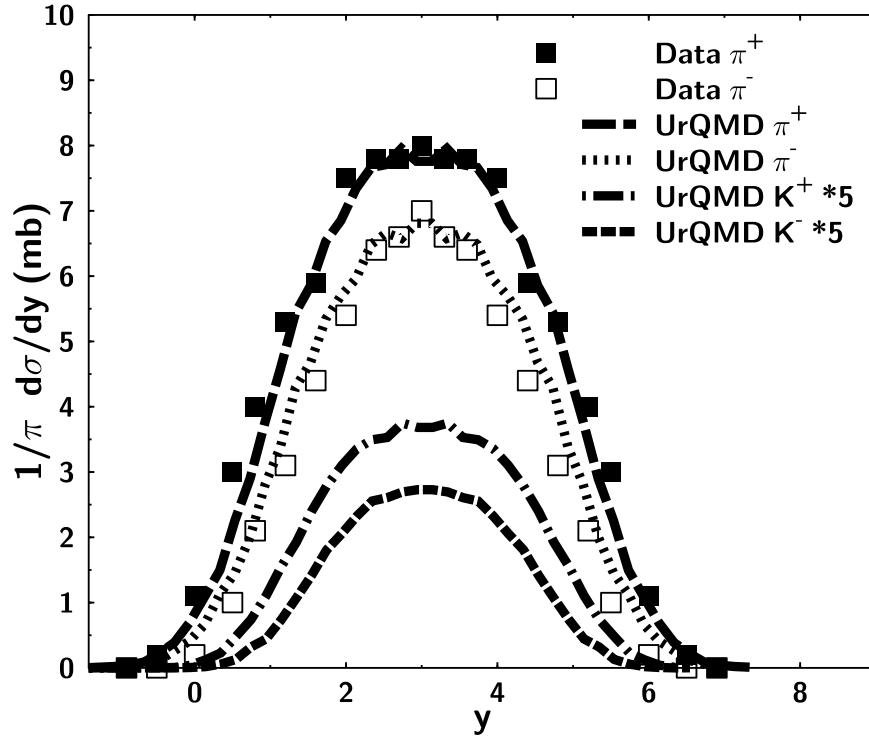


FIG. 31. Rapidity distribution of π^+ and π^- in pp collisions at 205 GeV/ c . Data are taken from [52].

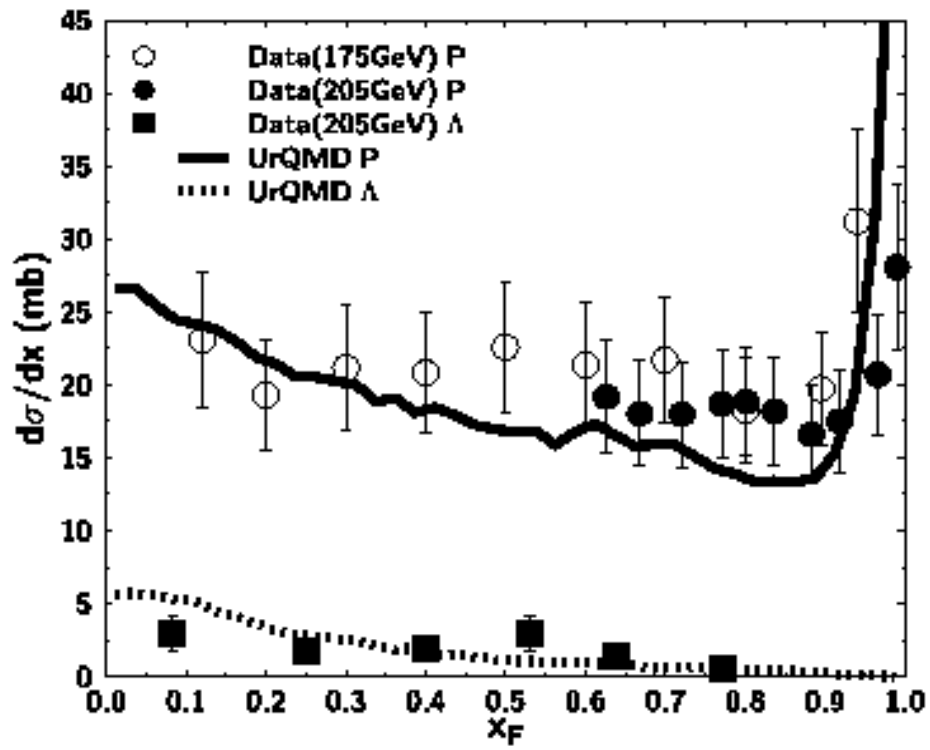


FIG. 32. $d\sigma/dx_F$ distribution of protons and Λ 's in pp collisions at 205 GeV/ c . Data are taken from [52].

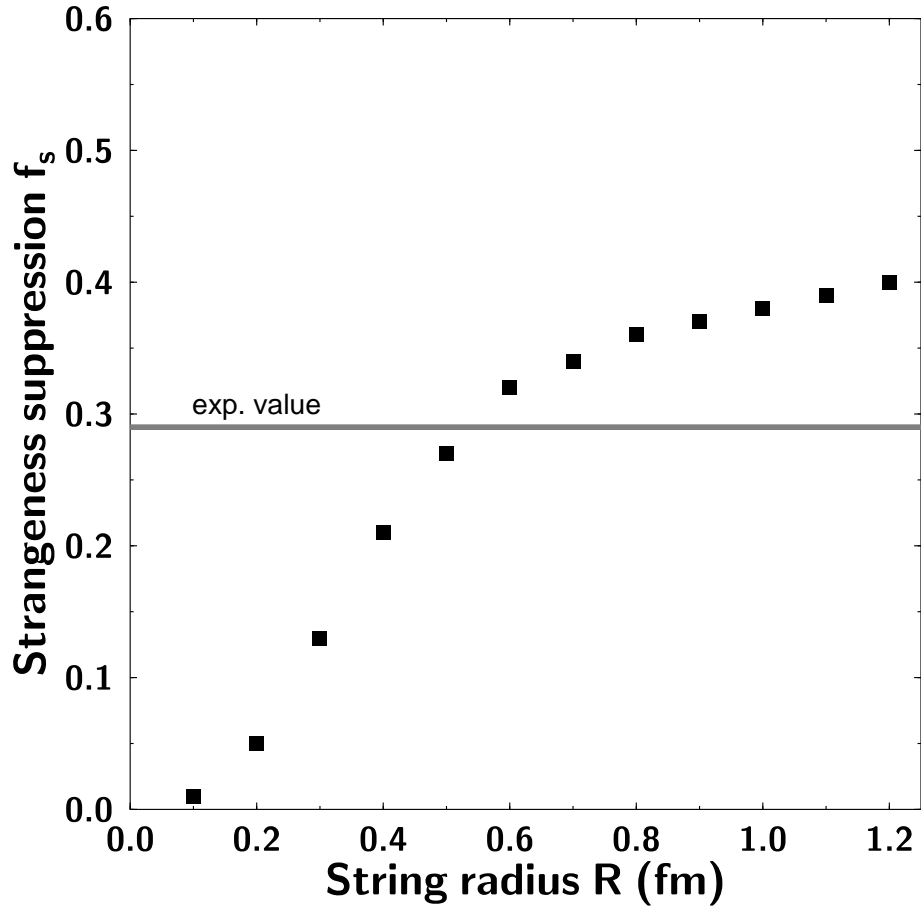


FIG. 33. Strangeness suppression f_s due to a finite transverse string radius R [46].

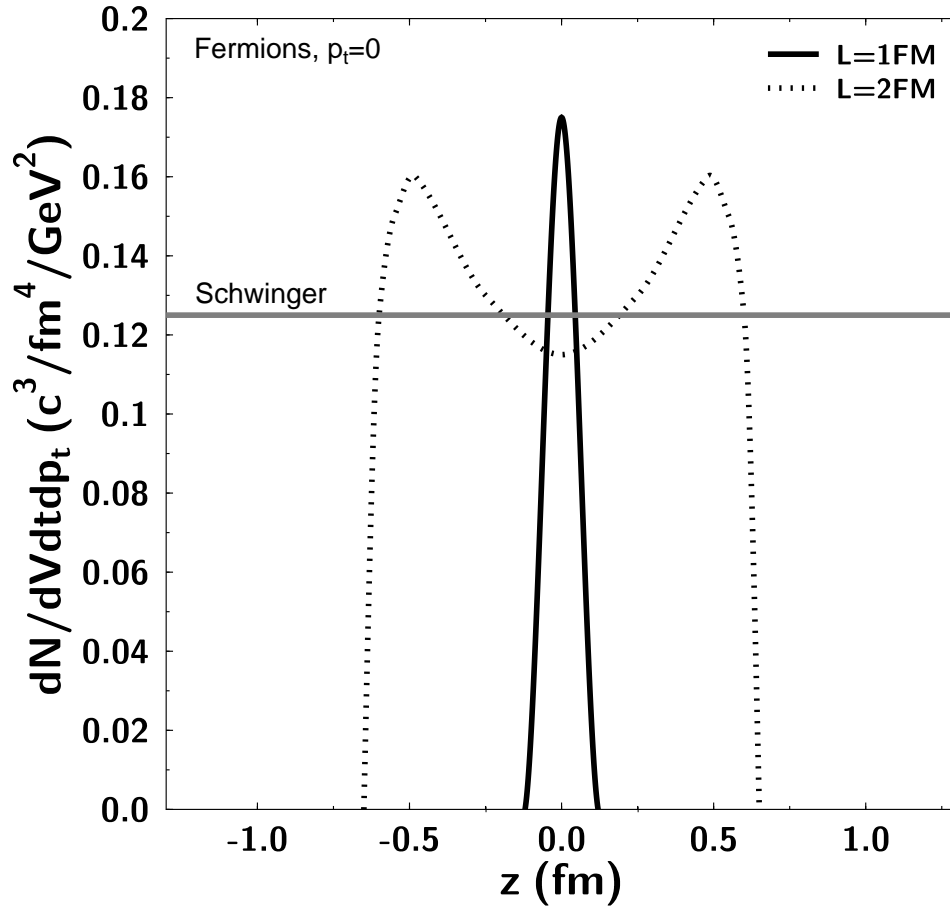


FIG. 34. Pair production rate in a finite color field as a function of the longitudinal field extension z [47].

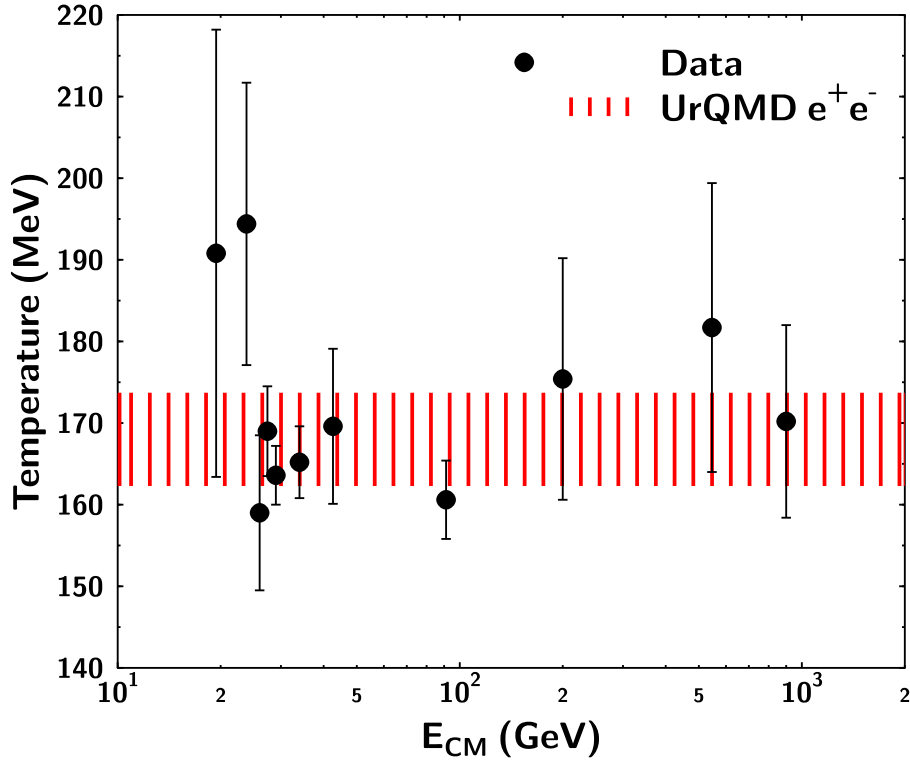


FIG. 35. Pion 'temperatures' (inv. slope parameter of the p_t distribution) extracted from e^+e^- annihilations in the UrQMD model for different energies are shown. They are compared to freeze-out 'temperatures' extracted from a statistical model fit to particle yields [50] in pp , $\bar{p}p$ and e^+e^- reactions.

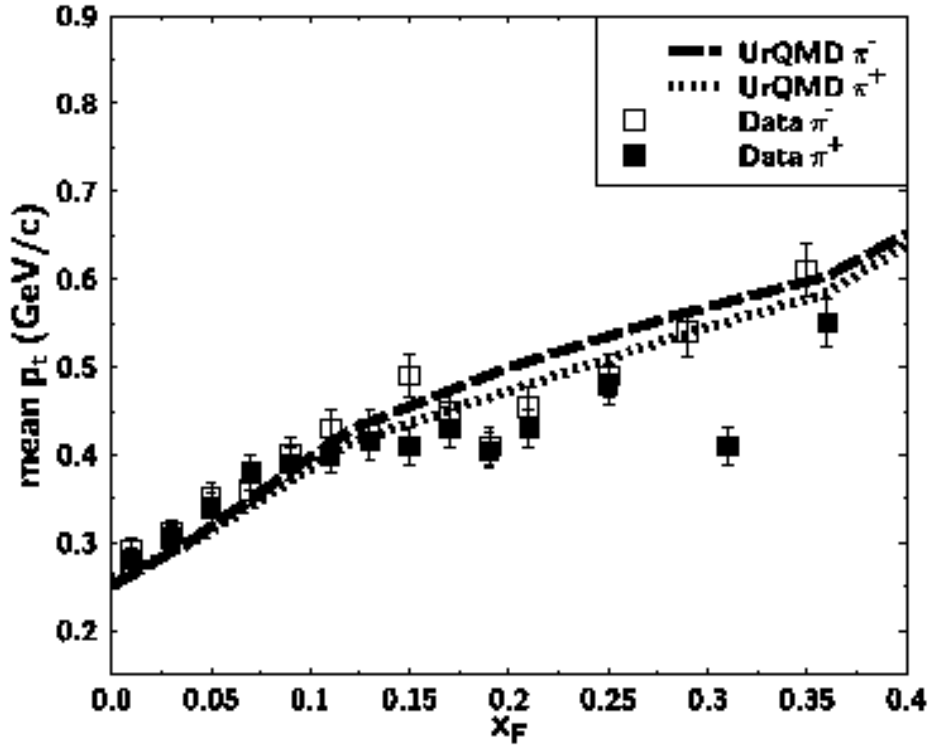


FIG. 36. Mean transverse momentum of π^+ (dotted line) and π^- (dashed line) in pp collisions at 205 GeV/c as a function of x_F . Data (π^+ 's, open squares, and π^- 's, full squares) are taken from [52].

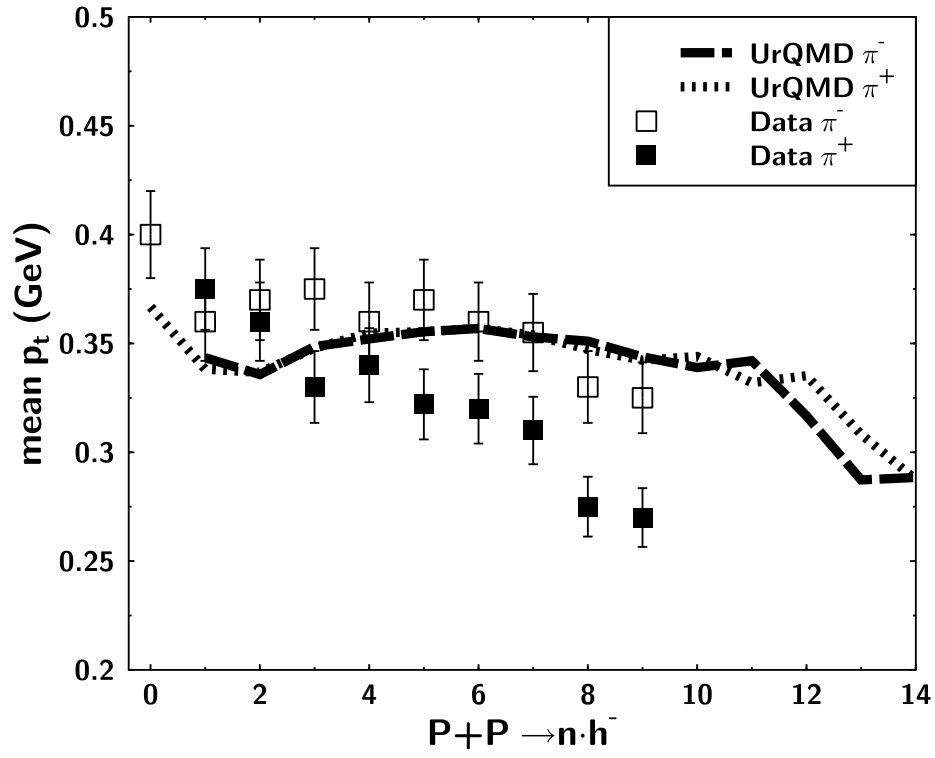


FIG. 37. The mean transverse momentum of π^\pm 's as a function of number of negatively charged hadrons in the reaction $p(205 \text{ GeV})+p$. Note the suppressed zero. Data are taken from [52].

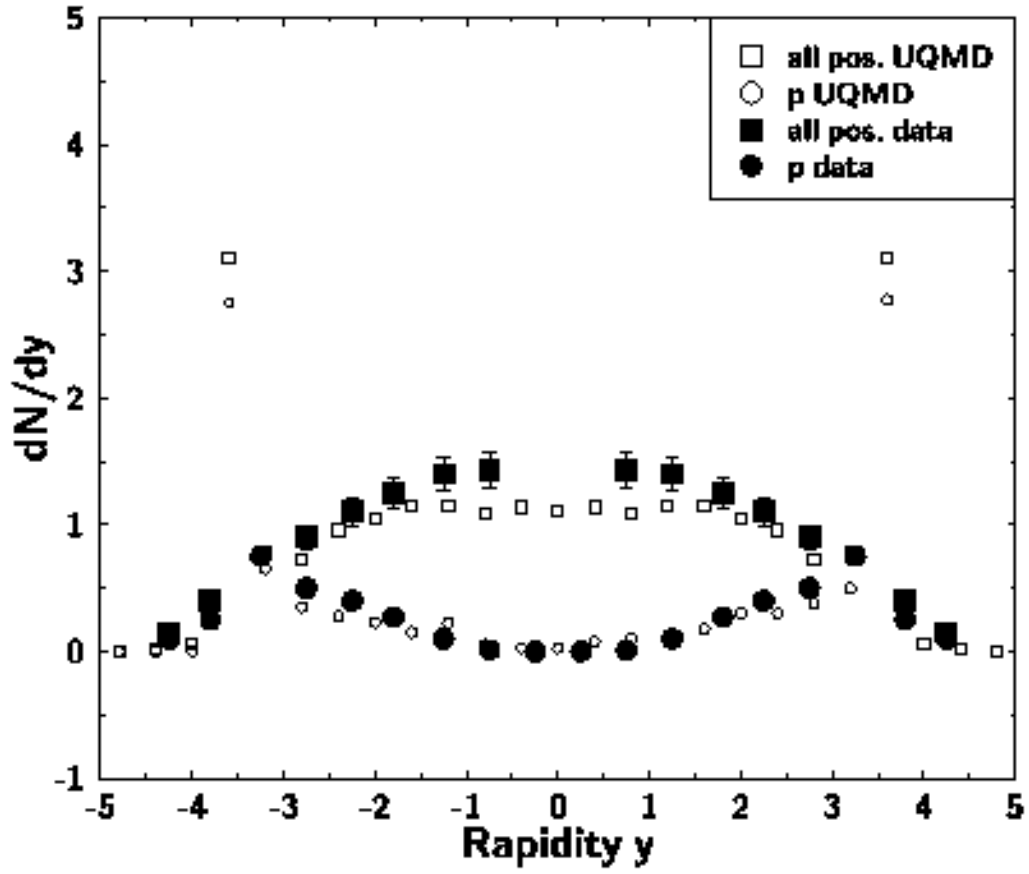


FIG. 38. Rapidity distribution of protons and positively charged particles for the reaction He+He at $\sqrt{s} = 31$ AGeV compared to data [53].

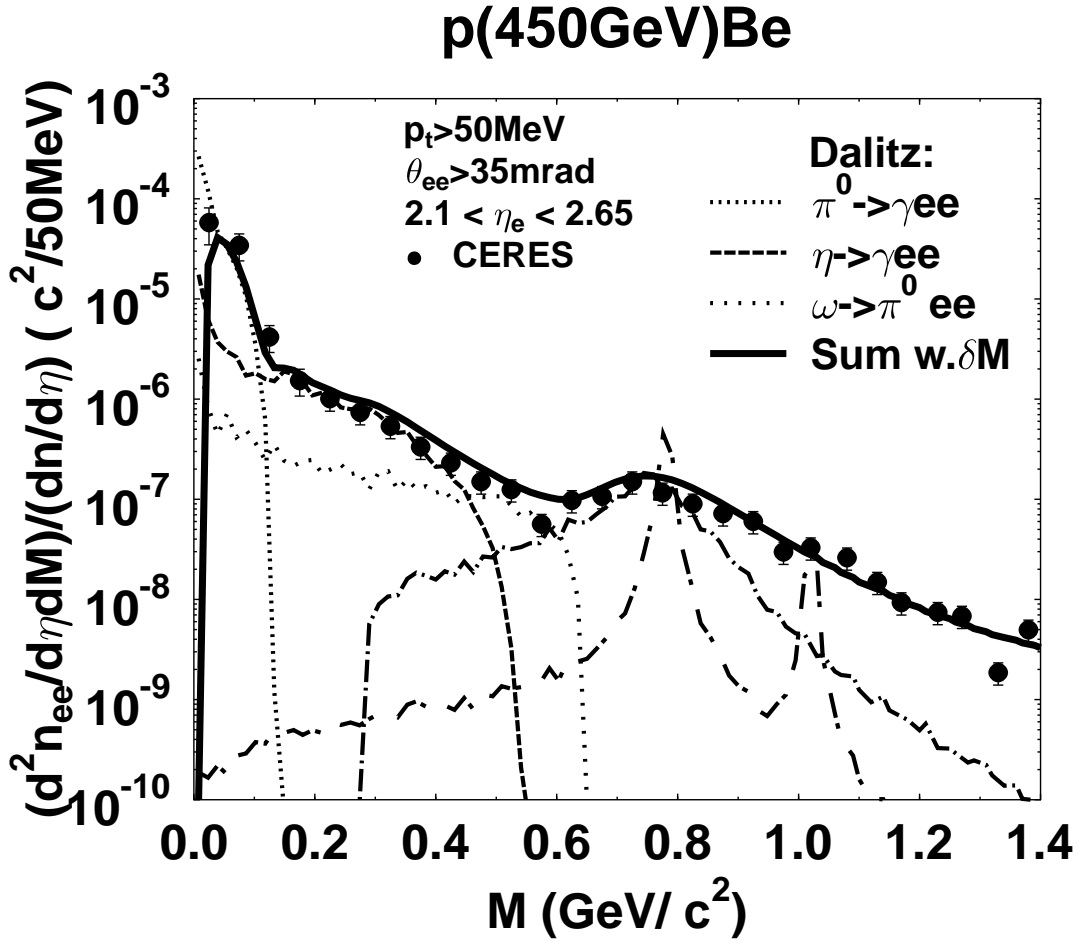


FIG. 39. Dilepton mass spectrum for $p+\text{Be}$ at 450 GeV/ c . The calculation includes Dalitz decays and conversion of vector mesons. Only the curve labeled sum of all contributions (solid curve) is folded with the mass resolution of the CERES (full circles) experiment [55].

TABLES

TABLE I. Baryons and baryon resonances implemented in the UrQMD model. All baryons up to $2.25 \text{ GeV}/c^2$ as well as their antiparticles are included.

N (Nucleon)	Δ (Delta)	Λ (Lambda)	Σ (Sigma)	Ξ (Xi)	Ω (Omega)
N_{938}	Δ_{1232}	Λ_{1116}	Σ_{1192}	Ξ_{1317}	Ω_{1672}
N_{1440}	Δ_{1600}	Λ_{1405}	Σ_{1385}	Ξ_{1530}	
N_{1520}	Δ_{1620}	Λ_{1520}	Σ_{1660}	Ξ_{1690}	
N_{1535}	Δ_{1700}	Λ_{1600}	Σ_{1670}	Ξ_{1820}	
N_{1650}	Δ_{1900}	Λ_{1670}	Σ_{1775}	Ξ_{1950}	
N_{1675}	Δ_{1905}	Λ_{1690}	Σ_{1790}		
N_{1680}	Δ_{1910}	Λ_{1800}	Σ_{1915}		
N_{1700}	Δ_{1920}	Λ_{1810}	Σ_{1940}		
N_{1710}	Δ_{1930}	Λ_{1820}	Σ_{2030}		
N_{1720}	Δ_{1950}	Λ_{1830}			
N_{1900}		Λ_{2100}			
N_{1990}		Λ_{2110}			
N_{2080}					
N_{2190}					
N_{2200}					
N_{2250}					

TABLE II. Parameters of the CERN-HERA fit [15] used in UrQMD for the total and elastic cross-section above the resonance region ($p_{lab} > 2 \text{ GeV}/c$). The cross sections are parametrized as: $\sigma_{\text{tot,el}}(p) = A + B p^n + C \ln^2(p) + D \ln(p)$, with the laboratory momentum p in GeV/c and the cross-section σ in mb.

σ	A	B	C	D	n
pp (total)	48.0	0.	0.522	-4.51	0.
pp (elastic)	11.9	26.9	0.169	-1.85	-1.21
pn (total)	47.3	0.	0.513	-4.27	0.
$\bar{p}p$ (total)	38.4	77.6	0.26	-1.2	-0.64
$\bar{p}p$ (elastic)	10.2	52.7	0.125	-1.28	-1.16
γp (total)	0.147	0.	0.0022	-0.017	0.
$\pi^+ p$ (total)	16.4	19.3	0.19	0.	-0.42
$\pi^+ p$ (elastic)	0.	11.4	0.079	0.	-0.4
$\pi^- p$ (total)	33.0	14.0	0.456	-4.03	-1.36
$\pi^- p$ (elastic)	1.76	11.2	0.043	0.	-0.64
$K^+ p$ (total)	18.1	0.	0.26	-1.	0.
$K^+ p$ (elastic)	5.0	8.1	0.16	-1.3	-1.8
$K^+ n$ (total)	18.7	0.	0.21	-0.89	0.
$K^- p$ (total)	32.1	0.	0.66	-5.6	0.
$K^- p$ (elastic)	7.3	0.	0.29	-2.4	0.
$K^- n$ (total)	25.2	0.	0.38	-2.9	0.

TABLE III. Baryon-baryon cross-sections in [mb] from the Additive Quark Model. NN scattering is explicitly treated, i.e. \sqrt{s} -dependent, etc.

$B_1 B_2$	N	Λ	Ξ	Ω
NN	40.0	34.7	29.3	24.0
$N\Lambda$	34.7	30.0	25.4	20.8
$N\Xi$	29.3	25.4	21.5	17.6
$N\Omega$	24.0	20.8	17.6	14.4

TABLE IV. Meson-baryon cross-sections in [mb] from the Additive Quark Model. MB scattering in the resonance region ($\sqrt{s} < 1.7 \text{ GeV}$) is explicitly treated.

$M_1 B_2$	N	Λ	Ξ	Ω
π	26.6	23.1	19.6	16.0
K	21.3	18.5	15.6	12.8
Φ	16.0	13.9	11.7	9.6

TABLE V. Meson-Meson cross-sections in [mb] from the Additive Quark Model. MM scattering in the resonance region ($\sqrt{s} < 1.7$ GeV) is explicitly treated.

$M_1 M_2$	π	K	Φ
π	17.8	14.2	10.7
K	14.2	11.4	8.5
Φ	10.7	8.5	6.4

TABLE VI. Mixing angles of meson multiplets according to the flavor SU(3) quark model: these parameters assign the pure $u\bar{u}$, $d\bar{d}$, $s\bar{s}$, to the physical particles according to the SU(3) quark model. The flavor mixing angles are chosen according to quadratic Gell-Mann-Okubo mass formula [39]. For the scalar mesons this formula is not applicable, here an ideal mixing angle ($\tan(\theta) = 1/\sqrt{2}$) is assumed.

Multiplet	degree
scalar	35
pseudoscalar	-10
vector	39
pseudovector	51
tensor	28

TABLE VII. Particle multiplicities from the UrQMD per inelastic pp event at 12 GeV/ c . Data are taken from [51].

Particle	UrQMD	Exp. Data
π^+	1.22	1.44±0.02
π^-	0.64	0.71±0.02
K_s^0	0.019	0.019±0.001
p	1.38	1.27±0.02
Λ	0.025	0.037±0.001

TABLE VIII. Particle multiplicities from the UrQMD per inelastic pp event at 205 GeV/ c . Data are taken from [52].

Particle	Exp. Data	UrQMD	Particle	Exp. Data	UrQMD
π^-	2.62±0.06	2.57	π^+	3.22±0.12	3.10
π^0	3.34±0.24	3.11	K^+	0.28±0.06	0.26
K^-	0.18±0.05	0.16	K^0		0.24
\bar{K}^0		0.16	K_S^0	0.17±0.01	0.20
$\Lambda + \Sigma_0$	0.096±0.01	0.16	$\bar{\Lambda} + \bar{\Sigma}^0$	0.013±0.004	0.037
p	1.34±0.15	1.32	\bar{p}	0.05±0.02	0.06

TABLE IX. Particle multiplicities from the UrQMD per inelastic pp event at $\sqrt{s} = 27$ GeV. Data are taken from [58].

Particle	Exp. Data	UrQMD	Particle	Exp. Data	UrQMD
π^+	4.10 ± 0.26	3.79	π^0	3.87 ± 0.28	3.72
π^-	3.34 ± 0.20	3.16	K^+	0.33 ± 0.023	0.31
K^-	0.22 ± 0.015	0.22	K_S^0	0.23 ± 0.015	0.26
η	0.39 ± 0.075	0.36	ρ_0	0.385 ± 0.056	0.50
ρ^+	0.552 ± 0.129	0.52	ρ^-	0.355 ± 0.091	0.41
ω	0.39 ± 0.026	0.47	K^{*+}	0.132 ± 0.018	0.13
K^{*-}	0.088 ± 0.013	0.080	K^{*0}	0.119 ± 0.023	0.123
\bar{K}^{*0}	0.09 ± 0.017	0.081	ϕ	0.019 ± 0.002	0.009
$f_2(1270)$	0.092 ± 0.013	0.119	p	1.20 ± 0.119	1.32
\bar{p}	0.063 ± 0.003	0.088	$\Lambda + \Sigma^0$	0.125 ± 0.016	0.19
Λ		0.15	Σ^0		0.041
$\bar{\Lambda} + \bar{\Sigma}^0$	0.020 ± 0.005	0.047	$\bar{\Lambda}$		0.038
$\bar{\Sigma}^0$		0.009	Σ^+	0.048 ± 0.019	0.050
Σ^0		0.041	Ξ^-		0.0041
Ξ^+		0.0053	Σ^-	0.013 ± 0.009	0.015
Δ^{++}	0.218 ± 0.016	0.235	Δ^0	0.141 ± 0.019	0.197
$\bar{\Delta}^{++}$	0.013 ± 0.005	0.016	$\bar{\Delta}^0$	0.034 ± 0.009	0.026
Σ^{*+}	0.020 ± 0.004	0.040	Σ^{*0}		0.071
Σ^{*-}	0.010 ± 0.003	0.009			